INL/JOU-24-80158-Revision-0

Harnessing dimethyl ether with ultra-low-grade heat for scaling-resistant brine concentration and fractional crystallization

June 2024

John H. Lienhard, Zi Hao Foo, Akshay Deshmukh, Aaron D Wilson

Changing the World's Energy Future

Idaho National Laboratory

INL is a U.S. Department of Energy National Laboratory operated by Battelle Energy Alliance, LLC

INL/JOU-24-80158-Revision-0

Harnessing dimethyl ether with ultra-low-grade heat for scaling-resistant brine concentration and fractional crystallization

John H. Lienhard, Zi Hao Foo, Akshay Deshmukh, Aaron D Wilson

June 2024

Idaho National Laboratory
Idaho Falls, Idaho 83415

http://www.inl.gov

Prepared for the
U.S. Department of Energy
Under DOE Idaho Operations Office
Contract DE-AC07-05ID14517

Harnessing Dimethyl Ether with Ultra-Low-Grade Heat for Scaling-Resistant Brine Concentration and Fractional Crystallization

Zi Hao Foo[†,‡], Akshay Deshmukh[†], Aaron D. Wilson[§], John H. Lienhard[†,*]

[†] *Department of Mechanical Engineering, Massachusetts Institute of Technology, Cambridge, Massachusetts 02139, United States*

[‡] *Center for Computational Science and Engineering, Massachusetts Institute of Technology, Cambridge, Massachusetts 02139, United States*

[§] *Chemical Separations Group, Idaho National Laboratory, Idaho Falls, Idaho 83415, United States*

Abstract

Solvent-driven separations may enable scalable concentration of hypersaline brines, supporting a circular resource economy from the extraction of lithium and rare earth elements from spent battery and magnet leachates. This work analyzes a novel solvent-driven water extraction (SDWE) system employing dimethyl ether (DME) and ultra-low-grade heat for brine concentration and fractional crystallization. SDWE exploits DME's unique properties: 1) a low dielectric constant that promotes water solubility over charged solutes by a factor of 10^3, and 2) a high volatility that facilitate efficient DME reconcentration with ultra-low-grade heat. The techno-economic viability of SDWE is assessed with a computational framework that encompasses a liquid-liquid separator and a solvent concentrator. We integrate the extended universal quasichemical model with the virial equation of state to predict the compositions of the complex three-phase DME-water mixture at vapor-liquid and liquid-liquid equilibrium. Subsequently, we optimize the thermodynamic and economic performance of SDWE, by controlling the interstage flash pressure, heat source temperature, and the number of concentrating stages. DME-based SDWE concentrates an input saline feed to 5.5 M and regenerates over 99 % of the DME using ultra-low-grade heat below 50 °C, with a DME/water selectivity ratio of 125. Our calculations reveal that optimal performance is achieved at interstage flash pressures of 0.4 - 0.5 bar for heat source temperatures between 323 - 373 K, with improved exergetic efficiencies at lower temperatures. At a heat source temperature of 323 K and an interstage pressure of 0.489 bar, DME-driven SDWE achieves an optimal thermodynamic efficiency of 20.5 % and a projected specific cost of US$ 1.93 m^{-3}. These specific costs suggest that SDWE is competitive with commercialized thermal distillation technologies, while mitigating the traditional risks associated with scaling in heat and mass exchangers with hypersaline brines.

Keywords: Brine Concentration, Dimethyl Ether, Desalination, Fractional Crystallization, Ultra-Low-Grade Heat

*Corresponding author: lienhard@mit.edu

1. Introduction

Global water scarcity has had a cascading impact on essential human activities, threatening irrigation [1–3], energy generation [4, 5], and critical metals extraction for battery and magnet production [6, 7]. By concentrating hypersaline brines, freshwater can be reclaimed from industrial wastewater, thereby safeguarding existing freshwater supplies from the discharge of polluted effluents [8–12]. Furthermore, brine concentration is instrumental in the promotion of a circular resource economy, enabling the recycling of valuable critical materials such as lithium, nickel, cobalt, and rare earth elements from spent battery and magnet leachates [7, 9, 13, 14]. These critical minerals can also be valorized from various industrial waste brines, including mine tailings, by-products from hydrocarbon extraction processes, and leachates from recycling of semiconductor and electronic wastes [7, 14–16].

Hypersaline brines are usually complex mixtures of inorganic salts, essential metals, and sparingly soluble scalants, with total dissolved solid (TDS) concentrations that typically exceed 70 g L^{-1}. As a result, hypersaline brine treatment is challenged by the high osmotic pressures and the propensity for scaling and fouling on heat and mass exchangers [14, 17]. Membrane processes like reverse osmosis (RO), nanofiltration (NF) and electrodialysis (ED), despite being highly energy efficient, faces limitations in processing brines with high salinity due to the operational limits of existing membranes and pressure vessels [17, 18] (see Appendix A), and lacks solute-specific selectivity necessary for targeted ion extraction [19, 20]. The presence of high concentrations of scale-forming ions (e.g., sulfates and phosphates of calcium and magnesium) in these brines further hampers the performance of both thermal- and membrane-based desalination processes, including mechanical vapor compression, multi-effect distillation and advanced variants of RO and electrodialysis systems, leading to reduced effectiveness [21–23] and salt rejection capabilities [17, 19, 24–26].

As a solution to these issues, solvent-driven water extraction (SDWE) emerges as a potentially viable and efficient alternative to extract water and critical metals from hypersaline brines [7, 27–30]. In SDWE, the saline feed is mixed with a partially water-miscible organic solvent in a liquid-liquid separator, resulting in the formation of two distinct liquid phases [31–33]. Water is then extracted up to thermodynamic equilibrium across the organic-aqueous liquid interface, with the dissolved electrolytes remaining in the concentrated brine due to the low dielectric constant of the organic solvent [11, 12, 34, 35]. As water is extracted into the organic-rich liquid phase, fractional crystallization of sparingly soluble salts may occur in the aqueous-rich phase, such as the selective precipitation of cobalt and samarium from spent magnet leachates upon solvent injection [7]. Subsequently, the organic-rich phase, now laden with water, is physically separated and regenerated to produce both purified water and reconcentrated solvent [36, 37]. A key advantage of SDWE is the physical segregation of the critical mass transfer process of water extraction from downstream heat exchangers and membranes [24, 35, 38]. This significantly reduces the risk of scalant precipitation and foulant deposition on crucial system components, presenting a more sustainable and operationally efficient method to handle high-salinity brines [14, 38, 39].

Recent studies have explored various solvents for use in solvent-driven water extraction, aiming to enhance water recovery, improve salt rejection, and boost energy efficiency during solvent regeneration [16, 40–46]. In these studies, dimethyl ether (DME), a polar aprotic solvent, has shown considerable promise as an effective organic desiccant due to its partial water miscibility and molecular characteristics conducive to near-complete salt rejection and efficient recovery of water from the solvent [14, 24, 31, 47–49]. To date, DME has been experimentally validated to separate

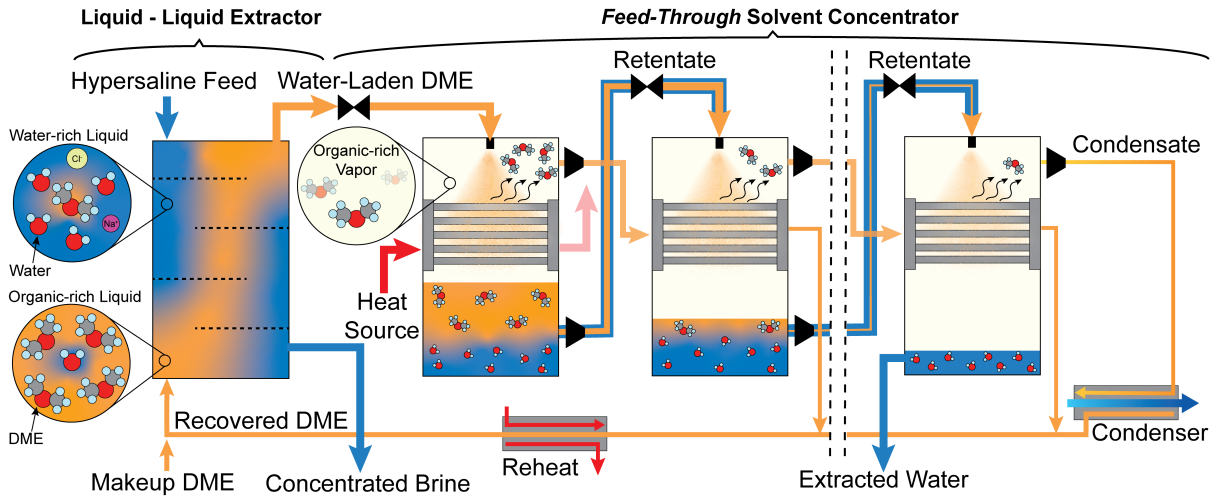

Figure 1: Schematic diagram illustrating a solvent-based water extraction system for brine concentration that is powered by ultra-low-grade heat. First, the hypersaline feed brine is contacted with liquefied dimethyl ether (DME) at a pressure above its vapor pressure in a liquid-liquid extractor [24]. Here, water is selectively extracted across a liquid-liquid interface between the bulk organic and aqueous feed streams, protecting the downstream heat and mass exchangers from scaling complications [14]. Next, the water-laden organic stream is siphoned out and concentrated with a regeneration stage. The organic stream is throttled, and heat from a thermal reservoir is supplied to enhance spontaneous DME vaporization. The low vapor-liquid-liquid equilibrium temperature of DME allows the use of ultra-low-grade heat ($T \leq 50°C$). The DME vapor is condensed in subsequent solvent concentration stages, and the recaptured latent heat is leveraged to vaporize additional DME from the retentate stream. The process is repeated until >99 % of the DME is recovered.

and recycle samarium and cobalt from spent magnet leachates [7], to fractionally crystallize calcium sulfate for aqueous waste descaling [31, 50], to extract water and produce a concentrated NaCl brine [24], and as a desiccant for the drying of biomass [51]. Recent experimental and molecular dynamics investigations suggest that dimethyl ether promotes fractional crystallization as an anti-solvent, by selectively extracting water from the aqueous-rich phase and inducing supramolecular saturation of the sparingly soluble salt [39, 46]. The properties of DME, notably its low dielectric constant ($\epsilon_{\text{DME}} < 5$), high volatility (vapor pressure > 5.9 bar at STP), and relatively low boiling point (269 K at 1 bar), are beneficial in minimizing the solubility and entrainment of inorganic electrolytes in the organic phase [31, 46, 52], allowing a circular solvent economy to be realized with thermally-driven systems. As illustrated in Fig. A.9, these distinct properties consequently enable the efficient regeneration of the solvent, which may be achieved with unconventional energy sources and ultra-low-grade heat [9, 32, 53].

Industrial activities such as drying, heating, and combustion produce waste heat in many forms, including vapors, fumes, exhaust gases, and wastewater [54, 55]. The chemical production and power generation sectors have attempted to harness waste heat for improved process efficiency, but a large proportion of it, often emanating from furnaces, motors, refrigeration systems, boilers, and other machinery, is unavoidably released into the environment [56–58]. Approximately 60 % of waste heat is categorized as ultra-low grade, with temperatures ranging between ambient and 80 °C [59, 60]. The properties of dimethyl ether, particularly its high volatility and low boiling point, enable DME-water mixtures to achieve vapor-liquid equilibrium at temperatures between 7 °C and 47 °C [47]. As shown in Fig. 1, these attributes make it feasible to use ultra-low-grade heat for reconcentrating DME following the extraction of water from hypersaline brines [14, 24].

In this study, we explore the technical and economic feasibility of using DME for solvent-driven water treatment

that is powered by ultra-low-grade heat sources. For brine concentration, an increased rate of DME feed maximizes water extraction [24], whereas fractional crystallization requires a precise, minimal introduction of DME to promote salt displacement in the aqueous-rich phase [7, 50]. Regardless of its application in brine concentration or fractional crystallization, the critical challenge remains that of DME regeneration from the organic-rich phase at liquid-liquid equilibrium[14]. Consequently, we focus on quantifying the energetic and economic cost of DME regeneration to facilitate a circular solvent economy, while employing NaCl mixtures as a model solution to elucidate the impact of feed salinity. We develop a multi-phase equilibrium model that integrates the extended universal quasichemical model [61–63] with the virial equation of state [64, 65] to accurately predict the composition of DME-water mixtures at both vapor-liquid and liquid-liquid equilibrium. Further, we examine the influence of various process variables, such as interstage flash pressure, heat source temperature, and the number of concentration stages, on the thermodynamic efficiency of the proposed SDWE unit. Finally, we conduct a preliminary techno-economic analysis to determine the specific cost of water recovery with our proposed DME solvent concentrator, comparing it with the anticipated costs of commercial thermal distillation technologies currently used in resource extraction from hypersaline brines.

2. Mathematical Model

2.1. Thermodynamic models for phase equilibrium calculations

In solvent-driven water extraction (SDWE) from brines, a polar aprotic solvent is first contacted with the saline feed solution, which selectively solvates water into the organic-rich stream, while retaining the inorganic solutes in the aqueous-rich stream in the liquid-liquid extractor (Fig. 2A) [24, 34, 38]. In this work, dimethyl ether (DME) is chosen due to its low polarity and strong ability to form asymmetric hydrogen bonds with water, an apposite combination that favors water solubility over charged ions by a factor of 10^3 [31, 46]. The salt rejection, water recovery and brine concentration ratios that are attainable by a liquid-liquid extractor is governed by the phase composition of the organic and aqueous-rich phases at thermodynamic liquid-liquid equilibrium (LLE) [35].

To achieve LLE in an isobaric - isothermal ensemble (NPT ensemble in statistical thermodynamics), isoactivity conditions between each chemical species present in both liquid phases must be satisified (see Appendix B for thermodynamic derivations). Mathematically, the isoactivity constraint can be expressed as:

$$\gamma_i^{aq,liq}(T, \boldsymbol{x}^{aq,liq})\ x_i^{aq,liq} = \gamma_i^{org,liq}(T, \boldsymbol{x}^{org,liq})\ x_i^{org,liq} \tag{1}$$

where $i \in \{H_2O$ (water), CH_3OCH_3 (dimethyl ether)$\}$, T [K] represents the equilibrium temperature at LLE, $\gamma_i^{aq,liq}$[-] and $\gamma_i^{org,liq}$ [-] represent the activity coefficient of species i in the aqueous- and organic-rich streams, $x_i^{aq,liq}$ [-] and $x_i^{org,liq}$ [-] denote the absolute mole fraction of species i in the aqueous- and organic-rich streams, respectively. Here, the species activity coefficients are calculated based on an excess Gibbs free energy formulation, which will be described in Section 2.1.1.

Following liquid-liquid extraction with DME, the water-laden organic-rich stream is siphoned out and passed into a solvent concentrator, as illustrated in Fig. 1. In the first stage, the water-laden DME stream is throttled to induce vapor-liquid (VLE) or vapor-liquid-liquid equilibrium (VLLE), and heat from a thermal reservoir is supplied to enhance spontaneous DME vaporization. In each subsequent solvent concentration stage, as depicted in Fig. 2B, the retentate stream from the previous stage is throttled, attaining VLLE (or VLE) at a temperature that is lower

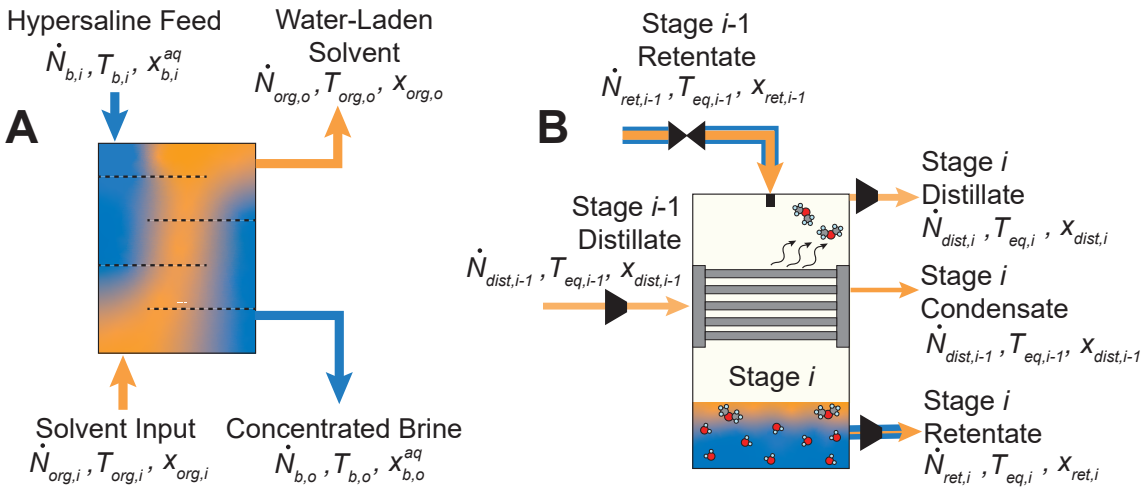

Figure 2: (A) Schematic diagram illustrating the molar flow rate, temperature and mole fraction of the input and output streams of the hypersaline feed brine and the organic solvent. The molar flow rate and mole fraction of the output organic and aqueous streams are calculated based on isoactivity thermodynamic constraints [24]. (B) Schematic diagram illustrating the material balance across the i^{th} stage of the solvent concentrator. Here, the retentate stream from the $(i-1)^{\text{th}}$ stage is throttled, attaining vapor-liquid-liquid equilibrium at a lower temperature, and establishing a temperature gradient across the heat exchanger. The distillate stream from the $(i-1)^{\text{th}}$ stage condenses within the lumen of the heat exchanger, and the latent heat is captured to distill DME from the retentate stream.

than the input distillate stream [46]. The distillate stream, consequently, condenses within the lumen of the heat exchanger, and the latent heat is captured to distill additional DME from the retentate stream [21]. Here, the high vapor pressure and volatility of DME allows VLE or VLLE to be attained at temperatures ranging between 280–305 K, enabling ultra-low-grade or waste heat sources (T $\leq$ 50°C) to be leveraged for the rapid and efficient recovery of DME [24]. The distillate and retentate temperatures, and the DME recovery ratio at each concentration stage is governed by the equilibrium compositions at VLE or VLLE.

For VLE, in an NPT ensemble, each chemical species present in the liquid and vapor phases must obey the isofugacity constraint (see Appendix B for thermodynamic derivations). Mathematically, the isofugacity constraint at VLE can be expressed as:

$$\gamma_i^{liq}(T, \boldsymbol{x}^{liq})\; x_i^{liq} P_i^{sat} = \phi_i^{vap}(T, P, \boldsymbol{x}^{vap})\; x_i^{vap} P \tag{2}$$

where $i \in \{\text{H}_2\text{O (water)}, \text{CH}_3\text{OCH}_3\text{ (dimethyl ether)}\}$, P_i^{sat} [Pa] denotes the saturation pressure of the pure species i, and ϕ_i^{vap} [-] represents the fugacity coefficient of species i in the vapor phase. The fugacity coefficients are estimated based on the virial equation of state, which will be discussed in Section 2.1.2. For VLLE, the isoactivity and isofugacity constraints (Eqs. 1 and 2) are solved simultaneously to obtain the equilibrium composition of the vapor, organic-rich and aqueous-rich liquid phases, as illustrated in Fig. 3.

2.1.1. Estimating species activity with the extended UNIQUAC equations

The extended universal quasichemical (eUNIQUAC) model is used to capture the thermodynamic non-idealities arising from solute-solute and solvent-solute interactions [61–63, 66]. The excess Gibbs free energy of the mixture is composed of: 1) a combinatorial term quantifying the entropic contributions from the mixing of solutes with varying sizes and shapes; 2) a residual term quantifying the enthalpic contributions from the solute-solute energetic

interactions and; 3) a Debye-Hückel term quantifying from the long-range electrostatic interactions between charged solutes. The eUNIQUAC equations are condensed in Eqs. 3–6.

$$G^{ex} = G^{ex}_{res} + G^{ex}_{comb} + G^{ex}_{DH} \tag{3}$$

$$\frac{G^{ex}_{res}}{RT} = \sum_i x_i \ln\left(\frac{\psi_i}{x_i}\right) + \frac{z}{2}\sum_i q_i x_i \ln\left(\frac{\theta_i}{\psi_i}\right) \tag{4}$$

$$\frac{G^{ex}_{comb}}{RT} = -\sum_i q_i x_i \ln\left(\sum_j \theta_j \tau_{ji}\right) \tag{5}$$

$$\frac{G^{ex}_{DH}}{RT} = \frac{4x_w M_w A_{DH}}{b^3_{DH}}\left[\ln\left(1 + b_{DH} I_m^{1/2}\right) - b_{DH} I_m^{1/2} + \frac{b^2_{DH} I_m}{2}\right] \tag{6}$$

where ψ_i [-] $= (x_i r_i)/(\sum_j x_j r_j)$, θ_i [-] $= (x_i q_i)/(\sum_j x_j q_j)$, τ_{ji} [-] $= \exp(-(u_{ji} - u_{ii})/T)$, I_m [mol m^{-3}] $= 0.5\sum_i m_i z_i^2$, A_{DH} [g mol^{-1}] $= 1.131 + (1.335 \times 10^{-3}) \times (T - T_0) + (1.164 \times 10^{-5}) \times (T - T_0)^2$ and b_{DH} [g mol^{-1}] $= 1.5$.

Subsequently, the rational activity coefficients can be calculated by taking the partial molar derivative of the excess Gibbs free energy, as described by Eqs. 7–8.

$$\ln\gamma_i = \ln\gamma_{i,res} + \ln\gamma_{i,comb} + \ln\gamma_{i,DH} \tag{7}$$

$$\begin{aligned} &= \ln\left(\frac{\phi_i}{x_i}\right) + 1 - \frac{\phi_i}{x_i} - \frac{z q_i}{2}\left[\ln\left(\frac{\phi_i}{\theta_i}\right) + 1 - \frac{\phi_i}{\theta_i}\right] \\ &\quad + q_i\left[1 - \ln\left(\sum_j \theta_j \tau_{ji}\right) - \sum_j \theta_j \frac{\tau_{ji}}{\sum_k \theta_k \tau_{kj}}\right] \\ &\quad + \left\{\frac{2A_{DH}M_w}{b^3_{DH}}\left[1 + b_{DH} I_m^{1/2} - (1 + b_{DH} I_m^{1/2})^{-1} - 2\ln(1 + b_{DH} I_m^{1/2})\right]\right\} \end{aligned} \tag{8}$$

where $\gamma_{i,res}$[-], $\gamma_{i,comb}$[-] and $\gamma_{i,DH}$[-] denote the activity coefficients from the residual, combinatorial and electrostatic contributions, respectively. The fidelity of the eUNIQUAC model in predicting the activity coefficients of water and DME have been documented in Fig. 3 and our prior publications [24, 66].

2.1.2. Calculating vapor fugacity with the virial equation of state

The virial equation of state is leveraged to calculate the fugacity coefficients of the species in the vapor phase at VLE and VLLE. Similar to the concept of activity coefficients, the fugacity coefficients quantify the deviations from thermodynamic ideality arising from solute-solute interactions in the vapor phase [65]. Here, fugacity coefficients are estimated based on the second virial coefficients, which are calculated using the method and mixing rules as proposed by Tsonopoulos [64], as depicted in Eqs. 9–14.

$$B_{i,i} = \frac{RT_{c,i}}{P_{c,i}}\left(f_i^{(0)}(T_{r,i}) + \omega_i f_i^{(1)}(T_{r,i}) + f_i^{(2)}(T_{r,i})\right) \tag{9}$$

$$B_{i,j}(T_{r,i,j}) = \frac{RT_{c,i,j}}{P_{c,i,j}}\left(f_i^{(0)}(T_{r,i,j}) + \omega_i f_i^{(1)}(T_{r,i,j}) + f_i^{(2)}(T_{r,i,j})\right) \tag{10}$$

$$f_i^{(0)}(T_{r,i}) = 0.1445 - 0.330 T_{r,i}^{-1} - 0.1385 T_{r,i}^{-2} - 0.0121 T_{r,i}^{-3} - 0.000607 T_{r,i}^{-8} \tag{11}$$

$$f_i^{(1)}(T_{r,i}) = 0.0637 + 0.331 T_{r,i}^{-2} - 0.423 T_{r,i}^{-3} - 0.008 T_{r,i}^{-8} \tag{12}$$

$$f_i^{(2)}(T_{r,i}) = a_i T_{r,i}^{-6} - b_i T_{r,i}^{-8} \tag{13}$$

$$\ln(\phi_i) = \left[\frac{2}{v_i}(x_i B_i + x_j B_{i,j})\right] - \ln\left(\frac{P v_i}{RT}\right) \tag{14}$$

where $B_{i,i}$ [-] and $B_{i,j}$ [-] denote the self and cross second virial coefficients, $T_{c,i}$ [K] and $P_{c,i}$ [Pa] represent the critical temperature and pressure of species i, $T_{r,i}$ [K^{-1}] denotes the reduced temperature of species i, v_i [m^3 mol^{-1}] denotes the molar volume of species i and ω_i [-] represents the accentricity factor of species i. The fugacity and activity coefficients have been used in conjunction to successfully correlate the phase compositions at VLE and VLLE, as illustrated in Fig. 3 and our prior publication [66].

2.2. Process models for system energy consumption

The thermodynamic performance of the proposed low temperature heat-driven DME extraction system is evaluated with a process model that has been implemented and solved with numerical algorithms in Python [67]. The enthalpy and entropy of the DME-water mixture necessary to evaluate the thermal and electrical energy consumption (see Section 2.2.1) are calculated based on the validated excess Gibbs free energy model. The process model (see Section 2.2.2) adheres to the core validated assumptions that have been widely used to evaluate thermal distillation systems for saline water desalination [21, 22, 68] and solvent regeneration [69, 70]. The sequence of numerical algorithms is summarized in Fig. D.10.

2.2.1. Calculating mixture enthalpy and entropy

When the water-laden DME stream exiting from the liquid-liquid extractor in Fig. 2A is flashed to a lower pressure, the DME-water mixture can separate into as many as three distinct phases at vapor-liquid-liquid equilibrium [47, 71, 72]. The three phases are the vapor, organic-rich liquid, and aqueous-rich liquid phases, which are abbreviated with the superscripts "*vap*", "*org,liq*" and "*aq,liq*", respectively. The mixture enthalpy for each of the three phases, at a given temperature, pressure and mole fraction, can be computed as the sum of pure component enthalpy and the excess enthalpy of mixing, as depicted in Eq. 15. The pure component enthalpy and entropy of water and DME are calculated using the Helmholtz free energy equation of state [73], as implemented in REFPROP [74].

The excess enthalpy of water and DME can be expressed in terms of the activity coefficients with the Gibbs-Helmholtz equation and subsequently calculated with the eUNIQUAC model [61]. Here, the partial molar derivative of the activity coefficient in Eq. 15 is calculated with a backward finite difference scheme. Similarly, the mixture entropy of the DME-water mixture in a given phase at VLLE can be calculated with the pure and excess entropies, as described in Eq. 16 [61].

$$H_{mix}^{(phase)} = \sum_i x_i^{(phase)} H_i^{(phase)} - RT^2 \sum_i x_i^{(phase)} \frac{\partial}{\partial T} \left(\ln \gamma_i^{(phase)} \right)_{P,x_i} \tag{15}$$

$$S_{mix}^{(phase)} = \sum_i x_i^{(phase)} S_i^{(phase)} - R \sum_i x_i \ln \left(\gamma_i^{(phase)} x_i^{(phase)} \right) \tag{16}$$

where $(phase) \in \{$"*vap*", "*org,liq*", "*aq,liq*"$\}$, $H_{mix}^{(phase)}$ [J mol^{-1}] and $S_{mix}^{(phase)}$ [J K^{-1} mol^{-1}] denote the mixture enthalpy and entropy of the DME-water mixture for a given phase at VLLE, and $H_i^{(phase)}$ [J mol^{-1}] and $S_i^{(phase)}$ [J K^{-1} mol^{-1}] represent the pure component enthalpy and entropy of species i. Thereafter, the total enthalpy and entropy of the DME-water mixture can be calculated by summing the contributions from the three distinct phases

at VLLE [75], as described in Eq. 17 and 18:

$$H_{mix} = \xi^{vap} H_{mix}^{vap} + (1 - \xi^{vap}) \xi^{org,liq} H_{mix}^{org,liq} + (1 - \xi^{vap})(1 - \xi^{org,liq}) H_{mix}^{aq,liq} \tag{17}$$

$$S_{mix} = \xi^{vap} S_{mix}^{vap} + (1 - \xi^{vap}) \xi^{org,liq} S_{mix}^{org,liq} + (1 - \xi^{vap})(1 - \xi^{org,liq}) S_{mix}^{aq,liq} \tag{18}$$

$$\xi^{vap} = \frac{N^{vap}}{N^{vap} + N^{org,liq} + N^{aq,liq}} \tag{19}$$

$$\xi^{org,liq} = \frac{N^{org,liq}}{N^{org,liq} + N^{aq,liq}} \tag{20}$$

where H_{mix} [J mol^{-1}] and S_{mix} [J K^{-1} mol^{-1}] represent the total enthalpy and entropy of a DME-water mixture at VLLE, and ξ^{vap} [-] and $\xi^{org,liq}$ [-] represent the vapor and organic-liquid quality at VLLE, respectively. We emphasize that the vapor and organic-liquid qualities are distinct from the mole fractions or compositions of the three phases. Here, as described in Eq. 19, the vapor quality is defined as the total molar amount of DME and water that exists in the vapor phase relative to the total molar amount of DME and water in the mixture [75]. The expression for vapor quality agrees with the conventional definition of quality at the vapor-liquid equilibrium of a pure species [75]; ξ^{vap} tends toward zero when no vaporization of the liquid occurs, and ξ^{vap} tends toward one as the mixture is fully vaporized. Similarly, as described in Eq. 20, the organic-liquid quality is defined as the total molar amount of DME and water that exists in the organic-rich phase relative to the total molar amount of DME and water in the collective liquid phases [75]; $\xi^{org,liq}$ approaches zero if the mixture only forms a single aqueous-rich liquid phase at equilibrium (VLE), and $\xi^{org,liq}$ approaches one if the mixture forms a single organic-rich liquid phase instead. Together, ξ^{vap} and $\xi^{org,liq}$ define the molar partitioning of a DME-water mixture in an equilibrium state.

2.2.2. Estimating distillate and retentate compositions with species and energy conservation

Here, we develop the process model that is used to estimate the thermodynamic efficiency and specific heat transfer area necessary for DME regeneration. This model leverages the same principles that have been widely adopted to simulate thermal distillation systems for water desalination [18, 21, 22, 33]. The assumptions include:

1. Steady-state operation across the throttling valves, heat exchangers, condensers and compressors.
2. The composition of the distillate and retentate streams are determined by the equilibrium compositions at vapor-liquid-liquid equilibrium.
3. The heat exchanger in each stage is sufficiently large to allow the full condensation of the input distillate stream (i.e., output vapor quality = 0).
4. Condensation of the distillate from the previous stage occurs isothermally at the saturation temperature within the lumen of the heat exchanger.
5. Negligible heat, energy and material are lost to the environment.
6. Negligible heat is generated by friction and similar losses.
7. The heat transfer coefficient is averaged over the length of the heat exchanger in each stage.
8. The thermodynamic properties of the DME-water mixture are constant in each stage and are a function of the stage temperature, pressure, and molar composition at equilibrium.

A schematic diagram of the heat-driven DME regeneration system is presented in Fig. 1, and the material and energy transport across each recovery stage is delineated in Fig. 2B. In each stage, the retentate stream from the

previous stage separates into vapor and liquid streams at VLLE or VLE. Under steady state operation, the total molar flux of the DME-water mixture is conserved between the input and the output retentate and distillate streams, as governed by Eq. 21. Further, the conservation of species requires that the molar flux of both species is constrained, as represented by Eq. 22:

$$\dot{N}_{ret,i-1} = \dot{N}_{dist,i} + \dot{N}_{ret,i} \tag{21}$$

$$\dot{N}_{ret,i-1} x_{ret,i-1} = \dot{N}_{dist,i} x_{dist,i} + \dot{N}_{ret,i} x_{ret,i} \tag{22}$$

where $x_{dist,i}$ [-] represents the composition of the vapor phase at VLLE/VLE, $x_{ret,i}$ represents the composition of the liquid phase at VLLE/LLE, and $\dot{N}_{dist,i}$ [mol s^{-1}] and $\dot{N}_{dist,i}$ [mol s^{-1}] denote the molar flux of the distillate and retentate streams for the i-th stage of the recovery system, as depicted in Fig. 2B. Based on the compositions at vapor-liquid equilibrium, the distillate vapor has a DME purity that exceeds 99 % [47, 71, 72]. The distillate stream exiting from the $(i-1)$-th concentration stage enters the lumen-side of the heat exchanger in the i-th concentration stage, where it subsequently condenses to form a saturated liquid. The latent heat of condensation is re-captured to distill additional DME from the retentate stream, as described by Eq. 23:

$$\dot{Q}_{latent,i} = \dot{H}_{ret,i-1}(T_{eq,i}, \xi^{vap} = 1) - \dot{H}_{ret,i}(T_{eq,i}, \xi^{vap} = 0) \tag{23}$$

where $\dot{Q}_{latent,i}$ [J s^{-1}] represents the captured latent heat of vaporization from the i-th concentration stage.

In each concentration stage, the equilibrium temperature, and the vapor and organic-liquid qualities are solved simultaneously with a constrained trust-region optimization method that is implemented with the Scipy package in Python [67]. The optimization problem is formulated in Eq. 24, and includes the constraints on the equilibrium temperature, entropy change of the mixture and the conservation of the two species. The inputs to the optimizer include the final pressure following flashing, the initial enthalpy of the retentate stream and the latent heat released from the condensation of the distillate stream. The enthalpies and entropies of the output distillate and retentate streams from each concentration stage can be calculated based on the derived equilibrium temperature, and the vapor and organic-liquid qualities.

$$T_{eq,i}, \xi_i^{vap}, \ \xi_i^{org,liq} = \underset{T_{eq}, \xi^{vap}, \xi^{org,liq}}{\operatorname{argmin}} \left\{ \left| \dot{H}_{mix}(T_{eq}, \xi^{vap}, \xi^{org,liq}) - \left(\dot{H}_{mix}(T_{eq,i-1}, \xi_{i-1}^{vap}, \xi_{i-1}^{org,liq}) + \dot{Q}_{latent,i} \right) \right|_2 \right\} \tag{24}$$

$$\begin{aligned}
\text{s.t.} \quad & T_{eq,i} > T_{VLLE}(P_{eq,i}), \quad \text{for vapor-liquid equilibrium} \\
& T_{eq,i} < T_{VLLE}(P_{eq,i}), \quad \text{for liquid-liquid equilibrium} \\
& T_{eq,i} = T_{VLLE}(P_{eq,i}), \quad \text{for vapor-liquid-liquid equilibrium} \\
& \dot{N}_i = \left[\xi_i^{vap} x_i^{vap} + (1 - \xi_i^{vap}) \xi^{org,liq} x_i^{org,liq} + (1 - \xi_i^{vap})(1 - \xi_i^{org,liq}) x_i^{aq,liq} \right] \dot{N}_{mix} \\
& \dot{S}_{mix}(T_{eq,i}, \xi_i^{vap}, \xi_i^{org,liq}) > \dot{S}_{mix}(T_{eq,i-1}, \xi_{i-1}^{vap}, \xi_{i-1}^{org,liq})
\end{aligned}$$

where $T_{eq,i}$ [K] denotes the equilibrium temperature of concentration stage i, and ξ_i^{vap} [-] and $\xi_i^{org,liq}$ [-] represent the output vapor and organic-liquid quality in concentration stage i.

Lastly, the amount of thermal energy consumed to recover 99 % of the input DME can be calculated based on an energy balance across the first concentration stage, as described by Eq. 25

$$\dot{Q}_{in} = \dot{H}_{ret,1}(T_{eq,1}, x_{ret,1}) + \dot{H}_{dist,1}(T_{eq,1}, x_{ret,1}) - \dot{H}_{ret,0}(T_{eq,0}, x_{ret,0}) \tag{25}$$

where $\dot{Q}_{in}$ [J s^{-1}] represents the heat input from an external thermal reservoir in the first concentration stage.

In addition, electrical work is consumed to compress the distilled vapor in each concentration stage, and it is affected by boiling point elevation of DME. As a result of the favorable intermolecular interactions between DME and water, the chemical potential of DME is lowered in the liquid phase, thereby elevating the boiling point temperature of DME [22, 75]. The distilled DME vapor in each concentration stage, consequently, will be superheated by a temperature that is equal to the induced boiling point elevation [23]. To maintain the temperature difference between the condensate and retentate in subsequent concentration stages, the distillate streams are compressed to the saturation pressure of the superheated vapor [76, 77]. The total electrical work consumed is the sum of the compression work in all of the concentration stages and the pumping power required to circulate the liquid DME condensate stream back to the liquid-liquid separator, as described by Eq. 26

$$\dot{W}_{in} = \sum_{i}^{N_t} \frac{\dot{W}_{comp,i}}{\eta_{is}} + \sum_{i}^{N_t} \frac{\dot{N}_{cond,i} \Delta P_{flow}}{\rho_i \eta_{pump}} \tag{26}$$

where $\dot{W}_{in}$ [J s^{-1}] represents the electrical power consumption, $\dot{W}_{comp,i}$ [J s^{-1}] denotes the isentropic electrical power consumed in stage i, η_{is} [-] and η_{pump} [-] represent the isentropic efficiency of the compressor and the pump, and N_t [-] represents the total number of concentration stages. In accordance with literature conventions, we adopt $\Delta P_{flow} = 0.2$ bar, $\eta_{is} = 0.8$ and $\eta_{pump} = 0.9$ in this work [77, 78].

2.3. Performance metrics for system analysis

The temperature, vapor and organic-liquid quality, and thermal and electrical energy consumption at each concentration stage are calculated and used to evaluate the techno-economic viability of a DME-based solvent-driven water extraction system. We discuss the metrics for thermodynamic efficiency in Section 2.3.1 and framework for estimating the specific cost of water extraction in Section 2.3.2.

2.3.1. Metrics for thermodynamic efficiency

Here, following literature conventions [21, 32, 33, 77, 79], the specific thermal and electrical energy consumption are calculated with respect to the volume of water extracted after the last concentration stage, as described in Eq. 27 and 28

$$\mathrm{SEC_T} = \frac{\dot{Q}_{in}}{\dot{N}_{N_t}} \tag{27}$$

$$\mathrm{SEC_E} = \frac{\dot{W}_{in}}{\dot{N}_{N_t}} \tag{28}$$

where $\mathrm{SEC_T}$ [kWh m^{-3}] and $\mathrm{SEC_E}$ [kWh m^{-3}] denote the specific thermal and electrical energy consumption, respectively. The thermodynamic (Second Law) efficiency, which is defined here as the ratio of the least work of separation to the actual exergy consumed [18], is calculated from the thermal and electrical energy input, as described in Eq. 29

$$\eta^{II} = \frac{\dot{G}_{ret,0} - \left(\dot{G}_{ret,N_t} + \sum_{i=1}^{N_t} \dot{G}_{dist,i}\right)}{\dot{W}_{in} + \dot{Q}_{in} \eta^{I}_{rev}} \tag{29}$$

where η^{II} [-] denotes the thermodynamic (Second Law) efficiency relative to a reversible process. Here, $\eta^{I}_{rev}[-] = 1 - \frac{T_{ds}}{T_s}$ represents the Carnot efficiency of a reversible power generation cycle relative to a dead state temperature

(T_{ds} = 298.15 K), and is used to calculate the exergetic value of the heat input [18, 21, 78]. The Gibbs free energy of the respective streams is calculated from the mixture enthalpy and entropy, as previously described in Eq. 17 and 18. Lastly, the specific area necessary for DME regeneration is the cumulative sum of the heat transfer area in the concentration stages, as expressed by Eq. 30

$$A_{sp} = \frac{1}{\dot{N}_{ret,N_t}} \left[\frac{\dot{Q}_{in}}{U_1(T_{eq,source} - T_{eq,1})} + \sum_{i=2}^{k} \frac{\dot{Q}_{latent,i}}{U_i(T_{eq,i-1} - T_{eq,i})} \right] \tag{30}$$

where A_{sp} [m^2 m^{-3}] represents the specific area per unit volume of water extracted, $\dot{N}_{ret,N_t}$ [mol s^{-1}] denotes the output flow rate of the recovered water, and U_i [W m^{-2} K^{-1}] represents the heat transfer coefficient, which is estimated based on the Nusselt number correlations proposed for corrugated heat exchangers [10, 21, 22]. Here, the specific area was chosen as the key metric to estimate capital costs of constructing thermally driven systems, in accordance with literature conventions [21, 68]. In this analysis, the heat exchanger area is derived from the latent heat required to vaporize the DME-rich solution, rendering the specific area of proposed solvent concentration system effectively independent of the heat source type.

2.3.2. Metrics for economic feasibility

In this work, we adapt a techno-economic model that has been used to investigate multi-effect distillation for zero-liquid discharge desalination to project the specific cost of DME recovery with our proposed system [21]. The hyperparameters of the techno-economic model are summarized in Appendix E. Here, the capital cost, which includes the cost of the pumps, compressors, heat exchangers, throttle valves and pipes, is assumed to scale linearly with the specific heat exchanger areas [21]. The net annual capital cost of the equipment is amortized over a period of 15 years and is normalized with an annuity factor (AF) that is calculated based on the prevailing interest rate of the central bank in a particular country, as expressed in Eq. 31 and 32

$$\text{CapEX}_{yr} = \frac{\sum_i C_i^{Cap}}{\text{AF } N_{ret,yr}} \tag{31}$$

$$\text{AF} = \frac{1 - \left(\frac{1}{1+r}\right)^T}{r} \tag{32}$$

where $C_i^{Cap} \in \{C_{pump}, C_{comp}, C_{hx}, C_{valve}, C_{pipe}\}$, CapEX_{yr} [US\$ m^{-3}] denotes the annual capital cost, r [-] represents the annual interest rate, AF [-] represents the annuity factor, and T [-] is the number of years for capital amortization. We note that the techno-economic model considers neither legal, permitting and siting, and consultancy costs, nor other indirect capital costs arising from insurance, contingency and freight, due to a dearth of publicly available information [21, 57, 80]. The operating cost is the sum of the cost of thermal and electrical energy consumption and estimated miscellaneous costs for chemicals (including make-up DME), labor and maintenance, as expressed in Eq. 33. The specific cost of water extraction is the sum of the capital and operating costs, as given by Eq. 34

$$\text{OpEX}_{yr} = \sum_i C_i^{Op} \tag{33}$$

$$C_{sp,yr} = \text{CapEX}_{yr} + \text{OpEX}_{yr} \tag{34}$$

where $C_i^{Op} \in \{C_{therm}, C_{elec}, C_{chem}, C_{labor}, C_{maint}\}$, and OpEX_{yr} [US\$ m^{-3}] represents the annual specific operating cost, and $C_{sp,yr}$ [US\$ m^{-3}] denotes the specific cost per unit volume of water extracted.

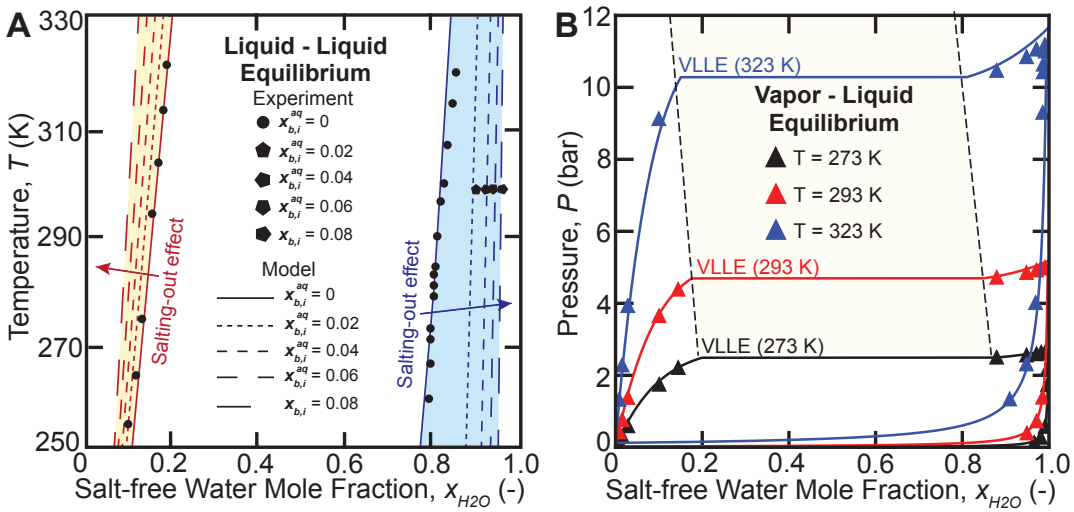

Figure 3: (A) Liquid-liquid equilibrium temperature as a function of the NaCl mole fraction and NaCl-free water mole fraction. The experimental data are obtained from Holldorff and Knapp [47] and McNally et al. [31]. The maroon and blue contoured lines represent the organic- and aqueous-rich phases, respectively. A prominent "salting-out" effect is observed in the presence of salt, which reduces the water uptake capacity of DME. (B) Plot of the vapor-liquid equilibrium pressure as a function of the NaCl-free water mole fraction. The experimental data are obtained from Holldorff and Knapp [47], and Pozo et al. [71, 72]. The beige area represents the region of vapor-liquid-liquid equilibrium.

3. Results and Discussion

3.1. Inducing spontaneous vaporization of dimethyl ether with small flash pressures

In solvent-driven water extraction, as illustrated in Fig. 1, the organic solvent first contacts a hypersaline feed stream in a counter-current liquid-liquid separator [24]. As delineated in our prior publication, a counter current liquid-liquid separator can be modeled with n equilibrium stages, where the aqueous- and organic-rich streams are in local liquid-liquid equilibrium (LLE) in each stage [24]. The water content of the DME-rich stream increases in each stage, as water is absorbed from the aqueous-rich across the liquid-liquid interface. Simultaneously, the water content in the aqueous-rich stream decreases, and the NaCl concentration consequently increases with increasing stages until it exits the liquid-liquid separator as a concentrated brine. Our prior experimental measurements show that DME selectively extracts water over NaCl into the organic-rich phase, as a result of its low dielectric constant of 5.34 at a temperature of 304 K [31]. The concentration of NaCl in the product organic-stream, consequently, is over three orders of magnitude lower than the NaCl concentration in the saline feed brine, and may fall below the detection limits of inductively coupled plasma optical emission spectroscopy (ICP-OES) for lower salinity feed solutions [24, 31, 46].

Even though NaCl does not partition readily into the DME-rich stream, the presence of inorganic solutes in DME-water mixtures has a profound impact on the equilibrium composition of the aqueous- and organic-rich phases at LLE (see Fig. 3A). Small inorganic charged solutes like NaCl hydrolyse readily in polar solvents like water, thereby reducing water's chemical potential in the aqueous-rich phase at equilibrium [81, 82]. The reduction in the chemical potential of water, consequently, facilitates a reduction of the water solubility in the DME-rich phase at LLE, which is a phenomenon known as the "salting-out" effect [46, 83]. For instance, as the NaCl mole fraction in the hypersaline feed stream increases from 0.02 (1.0 mol L^{-1}) to 0.08 (4.0 mol L^{-1}), the salt-free mole fraction

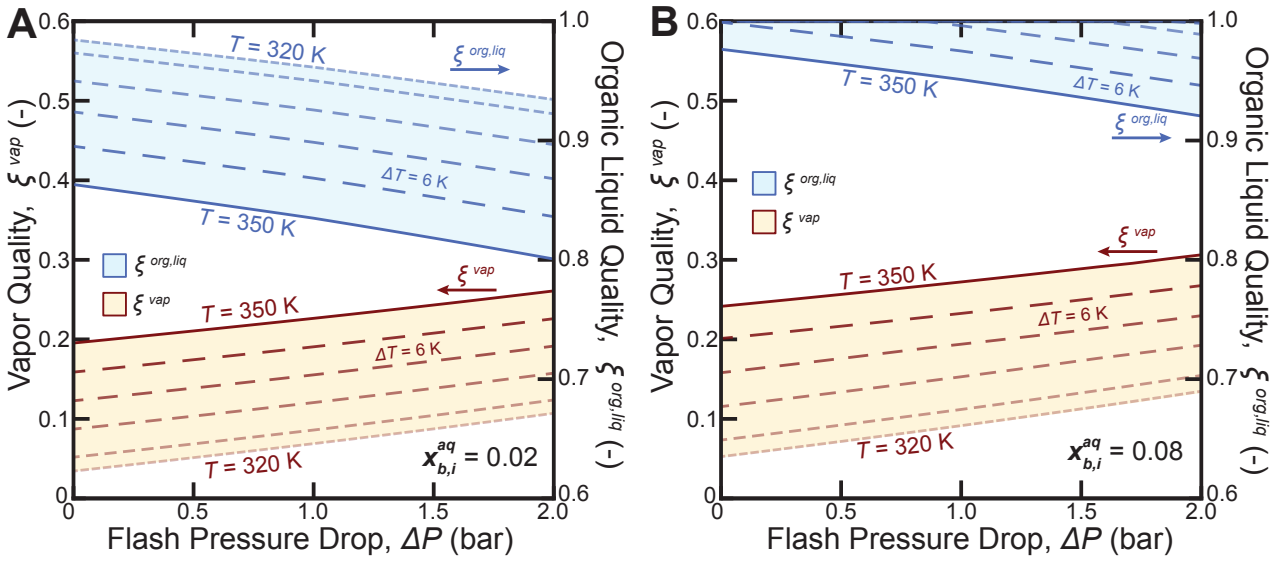

Figure 4: Vapor and organic liquid quality at vapor-liquid-liquid equilibrium for a dimethyl ether (DME) stream flashed from an initial pressure of 6 bar. The DME is the water-laden output organic stream from an upstream liquid-liquid extractor that has been contacted with a hypersaline NaCl brine at a mole fraction of: (A) 0.02; and (B) 0.08.

of DME in the aqueous-rich phase decreases from 0.092 to 0.037, while the modeled mole fraction of water in the organic-rich phase decreases from 0.140 to 0.090. As a consequence, the NaCl concentration of the saline feed stream limits the attainable water recovery in a liquid-liquid separator. This effect dictates the amount of DME recovery that is required after liquid-liquid extraction.

As illustrated in Fig. 1, a high purity DME stream can be regenerated from the water-laden organic-rich stream exiting from the liquid-liquid separator, through a series of heat-driven concentration stages. In this work, we aim to exploit the large differences in the volatility between water and DME for rapid and efficient organic solvent recovery following liquid-liquid extraction. Fig. 3B illustrates the phase compositions of a DME-water mixture at vapor-liquid and vapor-liquid-liquid equilibrium, as a function of the pressure and temperature [47, 71, 72]. The horizontal lines within the beige band depict the three phase (VLLE) region, while the upper and lower curves for each temperature represent the bubble and dew point curves, respectively. In other words, the DME-water mixture exists as a single liquid phase at pressures above the bubble point curve, and exists as a single vapor phase when the pressures are below the dew point curve. At a VLE temperature of 293 K, we observe that the DME composition of the vapor phase exceeds 99.5 %, at equilibrium pressures above 2 bar [47, 71, 72]. This large relative volatilty between DME and water can be leveraged to recover high purity DME at temperatures of 323 K or lower. Further, as the equilibrium temperature increases from 273 K to 323 K and greater, the purity of the DME vapor decreases from 99.5 % to 98 % over the same pressure intervals. As the temperature increases towards the boiling point of pure water, the relative volatilty between DME and water decreases, resulting in more water partitioning into the vapor phase at VLE [47]. Consequently, a more efficacious recovery of high purity DME is enabled with lower VLE/VLLE temperatures ($T \leq 50°C$), enabling the use of ultra-low-grade heat from low-temperature heat reservoirs [70, 78].

For a DME-water mixture that exists in VLE or VLLE, excess thermal energy must be supplied to enhance DME vaporization, by driving the equilibrium point rightward, to achieve >99 % DME recovery [21, 68, 84]. As discussed

in Section 2.2.1, the equilibrium point of a DME-water mixture at VLLE is defined by the vapor and organic-liquid qualities. Here, we stress that the vapor and organic-liquid qualities are distinct from the composition of the vapor and liquid phases at VLLE. The former defines the molar amounts of DME and water that exist in the vapor and organic-rich liquid phases, while the latter describes the ratio of DME relative to water in the vapor and liquid phases [75]. Fig. 4 illustrates the vapor and organic-liquid qualities of a DME-water mixture at vapor-liquid-liquid equilibrium, after the organic-rich stream exiting from the liquid-liquid separator is flashed without heat addition. Fig. 4A and B correspond to the output organic streams following water extraction from a saline feed with a NaCl mole fraction ($x_{b,i}^{aq}$) of: (A) 0.02 (1.0 M); and (B) 0.08 (4.0 M). The NaCl concentrations are selected to model the retentate streams from reverse osmosis [85] and minimal liquid discharge [86] applications.

From Fig. 4, we observe that a water-laden organic-rich stream exiting from the liquid-liquid separator at 6 bar can attain VLLE without external heat input at 320 K, achieving a vapor quality of 0.04 and 0.07 for $x_{b,i}^{aq} = 0.02$ and $x_{b,i}^{aq} = 0.08$, respectively with a 0.5 bar flash pressure; as temperature increases to 350 K, the vapor quality increases to 0.21 and 0.027, for $x_{b,i}^{aq} = 0.02$ and $x_{b,i}^{aq} = 0.08$ with the same flash pressure. The DME vaporization is driven entirely by the inherent enthalpy of the pressurized organic-rich mixture, an observation similar to that with ethanol-water mixtures [87, 88]. As equilibrium temperature increases from 320 K to 350 K, the enthalpy of the organic-stream increases proportionally, resulting in the observed enhancement of the vapor quality at a given flash pressure [68]. Similarly, the vapor quality at VLLE increases with increasing flash pressures because the enthalpy of the mixture's vapor phase decreases more rapidly with pressure as compared to the liquid phases [68, 78].

Further, we observe that the organic-liquid quality decreases with temperature and flash pressure, as illustrated in Fig. 4A and B. This observation demonstrates that DME is increasingly vaporized from the organic-rich liquid phase with higher temperatures and flash pressure, consistent with species conservation. While the results in Fig. 4 might suggest that DME may be recovered more facilely at higher temperatures and with greater flash pressures, the purity of the DME vapor decreases with temperature (see Fig. 3B). In essence, the LLE and VLE phase equilibrium behavior of DME-water mixtures suggests that system-scale performance would be highly sensitive to the flash pressure, heat source temperature and the NaCl mole fractions. The inherent interaction between the energy consumption and output DME purity is scrutinized over a range of independent variables in the system-scale analysis below.

3.2. Achieving high yield recovery of DME with ultra-low-grade heat sources

The accuracy of our computational model in predicting the system-scale energetic and economic performance rests on the fidelity of the activity and fugacity coefficient models in predicting thermodynamic equilibrium [9, 24, 33]. The juxtaposition between the predicted and experimental phase compositions at LLE, VLE and VLLE are shown in Fig. 3. The results indicate that the eUNIQUAC and virial equation of state models align with the experimental measurements to a large degree, registering a mean absolute error of 2.1 % and 3.2 % for the LLE and VLE experiments, respectively.

We next evaluate the feasibility of achieving high recovery of DME from the water-laden organic stream exiting from the upstream liquid-liquid extractor in Fig. 1. Fig. 5A illustrates the composition and temperature of the retentate and distillate streams, as a function of the number of concentration stages, at a fixed interstage flash pressure of 0.5 bar. Here, heat at 320 K is supplied to the first concentration stage. As illustrated in Fig. 2B, in each solvent concentration stage (stage i), the retentate stream from the previous stage (stage $i-1$) is throttled to attain

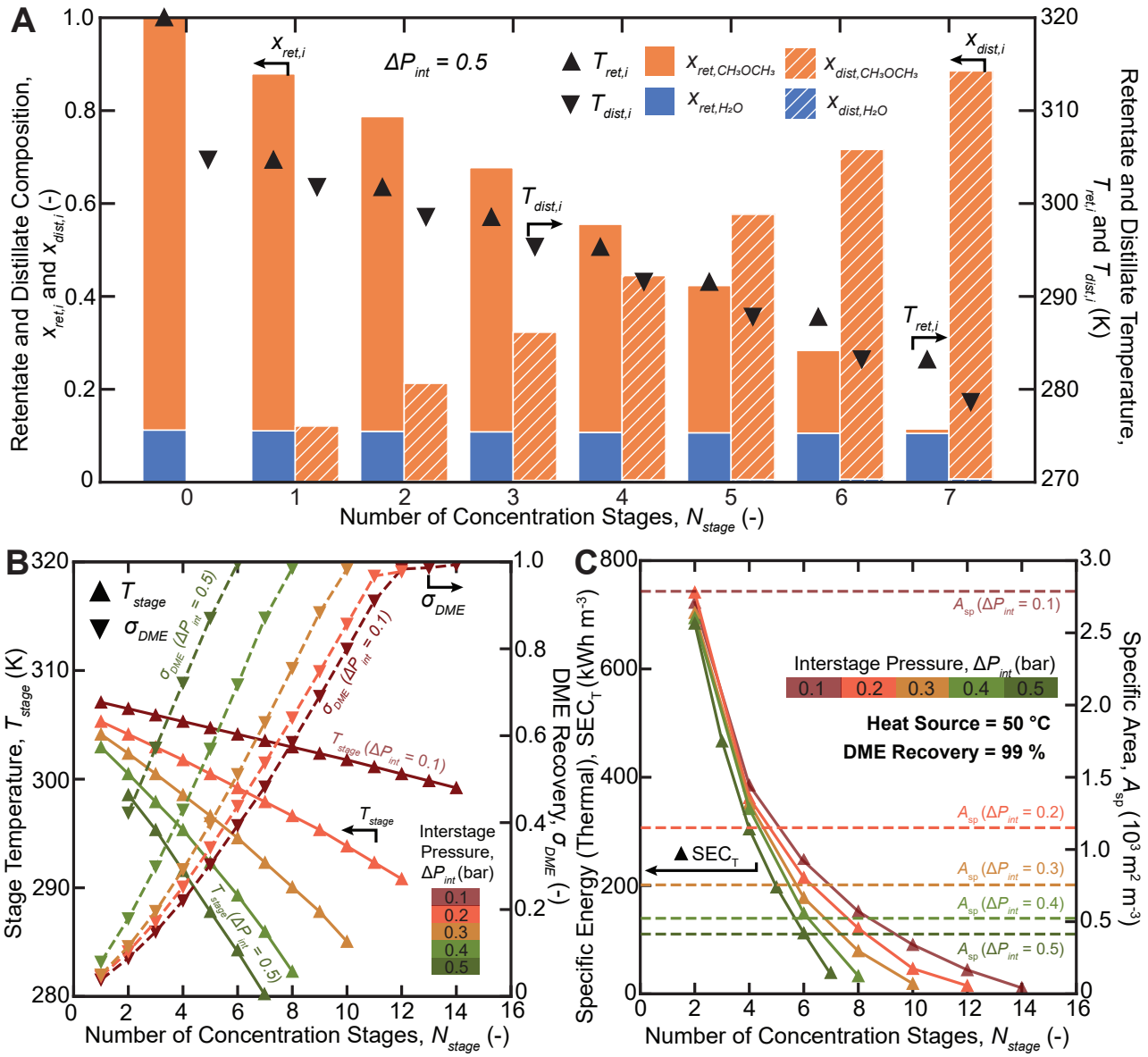

Figure 5: (A) Retentate and distillate composition and temperature as a function of the number of solvent concentration stages. Here, the heat transfer area is dictated by the temperature difference between the retentate and distillate streams. (B) Plot of the stage temperature and the DME recovery as a function of the interstage pressure and the number of recovery stages. (C) Plot of the specific thermal energy consumption and the specific area of the solvent concentrator as a function of the interstage pressure and the number of recovery stages.

VLLE at a lower temperature and pressure, and sprayed over a tube bundle in the shell-side of a heat exchanger. The distillate stream from the previous stage (stage $i-1$) condenses at a higher relative temperature within the tube-side of the heat exchanger, and the released latent heat of condensation vaporizes DME from the retentate stream in the shell-side. In this process, the temperature difference for heat transfer that exists between the distillate and retentate streams is controlled by the interstage flash pressure [21, 22], as depicted by the triangular markers in Fig. 5A. In other words, the interstage flash pressure generates the temperature difference that is necessary to recover the latent heat of condensation from the distillate stream in each stage. The retentate and distillate temperatures, consequently, decrease with stage count as a result of the reduced VLLE pressures from interstage flashing [68].

Further, the solid and hatched bars in Fig. 5A denote the composition of the retentate and distillate streams with increasing concentration stages. As expected, with increasing stage numbers, the molar quantities of DME and water in the retentate stream decrease, while the molar quantities of DME and water increase in the distillate stream. Notably, the molar flow rate of water in the retentate stream remains approximately constant, decreasing from 0.112 to 0.105 between the first and the last stage, while the molar flow rate of DME in the distillate stream increases from 0 to 0.878 over the same interval. The system exhibits a DME/water selectivity ratio of approximately 125 without the need for reflux or reboilers [75], attains a 99 % recovery of the DME from the input organic-rich stream, and achieves a recovered condensate stream DME purity of at least 99.3 %.

Fig. 5B illustrates the relationship between the stage temperature and DME recovery rate, and the interstage flash pressure and number of concentration stages. The upward and downward triangular markers represent the stage temperature and DME recovery for five interstage pressures, respectively. In agreement with the preceding paragraphs, the slope of the stage temperature curves increases with increasing interstage flash pressure, indicating that a larger temperature gradient is available to drive heat transfer between the distillate and retentate streams [21, 68]. In other words, a larger interstage flash pressure reduces the heat transfer area required to transfer a given amount of latent heat between the distillate and retentate streams. This phenomenon has a profound impact on the techno-economic performance of the system, as discussed below. Further, our results indicate that the number of stages required for 99 % recovery of DME decreases with increasing interstage flash pressure (ΔP_{int}). As illustrated in Fig. 5B, the minimum number of concentration stages for 99 % DME recovery drops from 14 to 7 when the interstage pressure increases from 0.1 bar to 0.5 bar.

Fig. 5C illustrates the specific thermal energy consumption as a function of the interstage pressure and the number of concentration stages. The comparisons in the figure are performed under the operating constraints of a temperature source at 320 K and a final DME recovery of 99 %. First, our computational results indicate that the specific thermal energy consumption (SEC_T) of the system decreases sharply with a larger number of concentration stages, across interstage pressures of 0.1 bar to 0.5 bar. The SEC_T decreases from 684.1 kWh m^{-3} to 36.6 kWh m^{-3} when the concentration stage count increases from 2 to 7, with an interstage flash pressure of 0.5 bar. Systems with a larger total stage count allow a larger proportion of the condensation latent heat from the distillate stream to be harvested for DME distillation [21, 22, 68]. The enhanced enthalpy recycling sharply reduces the amount of heat input that is necessary in the first concentration stage and minimizes the cooling load required in the final stage condenser (Fig. 1), yielding a synergistic reduction in the specific thermal energy consumption.

Further, our calculations indicate that the rate of decline in the SEC_T is more pronounced with larger operating interstage flash pressures. As discussed in Section 3.1, a larger interstage flash pressure enhances the spontaneous vaporization of DME from the retentate stream. Here, the quantity of DME that vaporized spontaneously increases by 36.6 % when the interstage flash pressure is raised from 0.1 bar to 0.5 bar, reducing the required heat input for high yield DME recovery, thereby corroborating the computational findings in Fig. 4.

The impact of interstage flashing and the concentration cycle count on the specific heat transfer area is illustrated on the right vertical axis in Fig. 5C. In agreement with the preceding paragraphs, systems that employ a larger interstage pressure require lower specific heat transfer areas, as a result of the larger temperature differences between the distillate and concentrate streams [68, 78]. For instance, the specific area decreases from a high of 2.79 $\times 10^3$

m^2 m^{-3} to 0.468 $\times 10^3$ m^2 m^{-3}, corresponding to an increment of ΔP_{int} from 0.1 bar to 0.5 bar. Cost effective thermal distillation systems, including multi-stage flash and multi-effect distillation, typically employ specific areas of up to 0.75 $\times 10^3$ m^2 m^{-3} to minimize capital costs [21, 22, 68]. The specific area of our proposed configuration lies within these conventional operating limits, which suggests that a heat-driven extraction system with DME may be economically viable for hypersaline brine concentration.

3.3. Optimizing process parameters for thermodynamic efficiency and specific cost

In the preceding sections, we demonstrated that the system-scale techno-economic performance is likely heavily influenced by the heat source temperature and the interstage flash pressure. Fig. 6A illustrates the thermodynamic (2nd Law) efficiency as a function of the flash pressure, for heat source temperatures of 323 K, 348 K and 373 K. The thermodynamic efficiency is the ratio of the least exergy of separation to the actual exergy consumed by thermal and electrical energy input [12, 21, 22]. As previously described in Section 2.2.2, thermal energy is consumed to drive DME vaporization in the first concentration stage, while electrical work is largely consumed for DME vapor compression in each concentration stage (if required). Our model suggests that the solvent extraction system can achieve thermodynamic efficiencies of 0.205, 0.112, and 0.080, leveraging heat from thermal reservoirs at 323 K, 348 K and 373 K, respectively. The computed thermodynamic efficiencies align with the reported values for multi-effect distillation and multi-stage flash systems operating with similar heat source temperatures [18, 21, 69, 70, 76].

Notably, across the three tested heat source temperatures, the results show that our proposed system attains a local optimum thermodynamic efficiency for interstage flash pressures of 0.4–0.5 bar. In general, thermal distillation systems (e.g., multi-stage flash) exhibit a decreasing thermodynamic efficiency with increasing flash pressures, as a consequence of the unavoidable entropy generation from the free expansion of a fluid in a throttling valve [68, 89]. Consequently, as illustrated in Fig. 6A, we observe a similar phenomenon, where the thermodynamic efficiency of the solvent concentration system increases from 0.024 to 0.205 at $T_s = 323$ K as the flash pressure falls from 1.0–0.5 bar (Effect 1). As exemplified in Fig. 6A, on the other hand, the ratio of electrical work to heat consumption decreases with increasing flash pressure. As the interstage flash pressure increases, a larger temperature difference is created between the distillate and retentate streams in each concentration stage, and less vapor compression work is consumed combating the adverse effects of boiling point elevation in the distillate stream. A unit of thermal energy from a low temperature reservoir at 323 K, 348 K and 373 K has an exergetic value that is 84.5 %, 78.8 % and 73.2 % lower than a unit of electrical work, respectively, relative to a dead state temperature of 298.15 K. [75]. The exergy consumption of the solvent concentrator, consequently, decreases in proportion with the decreasing electrical work consumption over the range of the interstage pressures from 0.1 bar to 0.5 bar (Effect 2). When the competing impacts of the irreversible entropy generation (Effect 1) and the exergy consumption (Effect 2) from interstage flashing are superimposed, therefore, a local maximum as observed in Fig. 6A in the thermodynamic efficiency is derived.

Fig. 6B illustrates the thermodynamic efficiency as a function of the heat source temperature for five interstage pressures ranging from 0.1 bar to 0.5 bar. In general, the thermodynamic efficiency increases with lower heat source temperatures because the exergy consumption per unit joule of heat decreases with temperature [75]. For instance, the thermodynamic efficiency increases from 0.109 to 0.239 as the heat source temperature declines from 350 K to 320 K with an interstage pressure of 0.5 bar. Further, the gradient of the thermodynamic efficiency with respect to the heat source temperature decreases with decreasing interstage temperature. As discussed in the previous

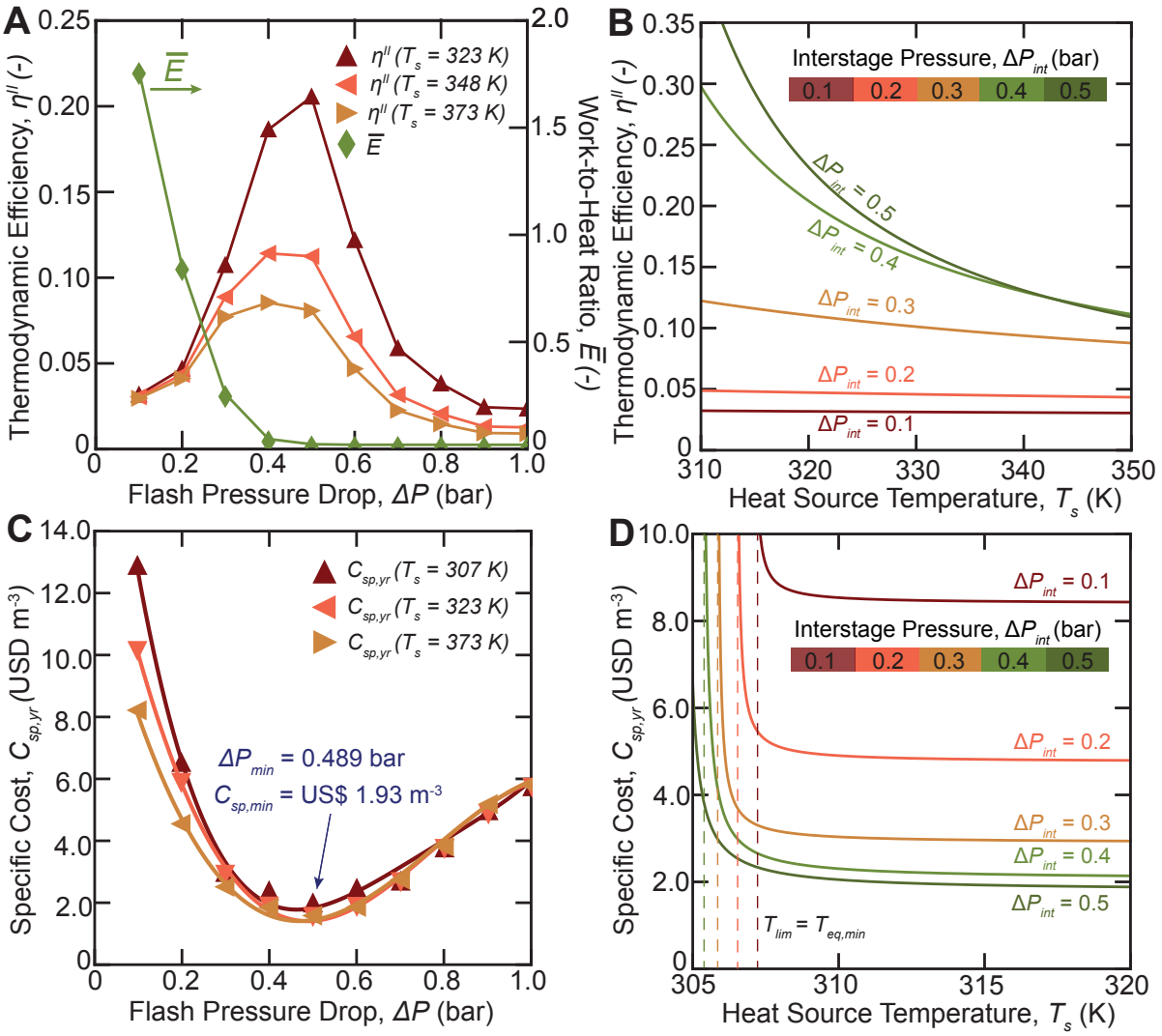

Figure 6: Thermodynamic (Second Law) efficiency of the solvent concentrator as a function of: (A) the interstage flash pressure; and (B) the heat source temperature. An optimal thermodynamic efficiency is observed for an interstage flash pressure of 0.4–0.5 bar, while a monotonically decreasing relationship to the heat source temperature is seen. Plot of the specific cost per unit volume of water extracted as a function of: (C) the interstage flash pressure; and (D) the heat source temperature. Similar to the relationships with the thermodynamic efficiency, an optimal specific cost is observed for an interstage flash pressure of 0.4–0.5 bar. The specific cost tends to infinity with lower temperature heat reservoirs as a consequence of divergence in the heat exchanger area.

paragraph, the ratio of work to heat consumption increases with smaller interstage pressures, shifting the process to be more electically-driven. The thermodynamic efficiency, consequently, becomes less variable with the temperature of the thermal reservoir for systems employing lower interstage pressures.

The influence of the interstage flash pressure on the specific cost of water recovery is illustrated in Fig. 6C, for heat source temperatures of 307 K, 323 K, and 373 K. We stress that the specific costs reported in this section correspond to the ideal production cost of water extraction, and do not include the profit margins and other additional business costs, as delineated in Section 2.3.2. Similar to the observations with the thermodynamic efficiency, our results suggest that there is a local minimum in the specific costs at an interstage pressure interval from 0.4 to 0.5 bar. Likewise, the local minimum in the specific cost is the result of a superposition of two effects: 1) the capital

cost declines with increasing interstage flash pressure, as the larger temperature gradient necessitates a smaller heat transfer area in each stage, and 2) the operational costs increases with increasing interstage flash pressure as a result of higher energy consumption from the reducing thermodynamic efficiency.

Fig. 6D depicts the specific cost of water recovery as a function of the heat source temperature, for five interstage pressures ranging from 0.1–0.5 bar. Our results suggest that the specific cost is fairly invariant to the heat source temperature when T_s exceeds 315 K across the five tested interstage pressures. This phenomenon is a result of the invariance of the capital costs, because the bulk of the heat exchanger area is defined by the temperature gradient between the distillate and retentate streams in stages 2 to N_T, as previously illustrated in Fig. 4A. As the heat source temperature decreases, however, we observe an asymptotic behavior with the specific cost in Fig. 6D, which diverges to infinity at a limiting temperature. The limiting temperature for each interstage pressure curve occurs at the equilibrium temperature in the first concentration stage. As the heat source temperature approaches the first equilibrium temperature, the requisite heat exchanger area and capital cost exponentially inflates, and consequently, the specific cost of water extraction diverges to infinity [21]. Although it has not been considered in this analysis, the reduced scaling tendency in heat exchangers with SDWE could permit the use of less corrosion-resistant and more cost-effective materials, further decreasing the specific costs as detailed in Fig. 6D.

In total, the analysis presented collectively in Fig. 6A–D illustrates the viable operating window of an ideal DME-based solvent concentration system. With a heat source temperature of 323 K, our model suggests that the locally minimized specific cost is US$ 1.93 m^{-3}, at an interstage pressure of 0.489 bar. In comparison, an ideal multi-effect distillation system for zero-liquid discharge desalination (i.e., a practical system that is otherwise not afflicted by scaling of heat and mass exchangers) exhibits specific costs between US$ 1.5 m^{-3} to US$ 2.2 m^{-3}, calculated based on similar thermodynamic and economic assumptions [21]. In other words, the similarity in specific costs with a commercialized brine concentration technology suggests that solvent-driven brine concentration could be economically effective for hypersaline water extraction.

3.4. Quantifying local interest rate and business cost impacts on the specific cost

Here, we illustrate the impact of the major constituents of the techno-economic model for the projected specific cost of water recovery. Once again, we emphasize that the techno-economic projection represents the ideal production cost of water recovery, and does not consider profit margins, consulting, legal, permitting and other unpredictable latent business costs that will influence the actual selling price at economic market equilibrium [3, 90].

Fig. 7 illustrates the projected specific cost of water for six countries with existing high salinity brine treatment industries, leveraging heat from a thermal reservoir at 323 K. The economic projections are conducted based on recently published techno-economic models for multi-effect distillation [21] and high salinity electrodialysis [3]. The interest rates, labor and energy costs are adapted from global surveys as of October 2023 (see Appendix E). The capital costs are amortized over a period of 15 years, and central bank interest rates are assumed. The total structural and equipment costs are assumed to scale linearly with the heat exchanger areas [21]. As expected, the specific cost of water recovery increases with feed salinity as the least work of separating water from a mixture rises, agreeing with previously published thermodynamic analyses [12, 23, 38, 78, 90].

Our economic estimates suggest that the capital costs of constructing a solvent-driven brine concentration facility are most heavily influenced by interest rates. For example, a larger fraction of the specific costs is attributed to

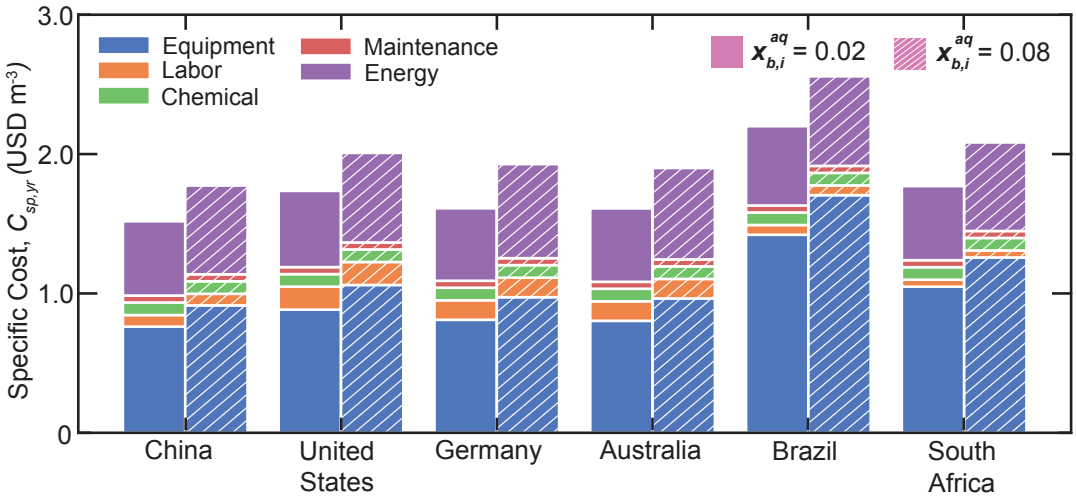

Figure 7: Specific cost per unit volume of water extracted with the DME-based system, operating with a heat source at 323 K and an interstage flash pressure of 0.5 bar. The techno-economic analysis is projected based on the prevailing central bank interest rates, and the estimated local labor, energy and chemical costs as of October 2023. The specific costs correspond to the estimated cost of recovering a cubic meter of water from a water-laden DME stream, following liquid-liquid extraction from a hypersaline brine feed with an initial NaCl mole fraction of: (A) 0.02; and (B) 0.08.

a higher amortized capital costs for Brazil, which has a central bank interest rate of 13.75 %, as compared to the United States interest rate of 5.5 %. Further, the techno-economic model assumes the availability of low-grade heat at a discounted price [55]; the specific cost of water is expected to rise by an estimated amount between US $ 0.50 m^{-3} to US $ 0.75 m^{-3} if high quality steam at 100 °C has to be employed [21].

Across the six modeled countries, the results suggest that the capital and operational costs have an impact comparable to the net specific costs. However, in practically sized systems, the presence of unforeseen fugitive losses in the retentate pressure and material leakage during throttling may reduce the thermodynamic efficiency, and increase the total energy consumption [68]. Nevertheless, the economic results appear to indicate that the specific cost of water production is comparable to commercialized brine concentration technologies when similar assumptions are adopted for the techno-economic projections [21, 78]. All in all, the preliminary techno-economic assessment suggests that the solvent-driven brine concentration system is potentially economically competitive for water extraction from hypersaline streams, warranting a deeper industrial consideration.

4. Implications for solvent-driven water extraction

In this study, we present a computational investigation of a novel dimethyl ether (DME)-based solvent-driven water extraction (SDWE) system, tailored for brine concentration and fractional crystallization applications. The energetic and techno-economic viability of the proposed SDWE system is analyzed with a system-scale computational model that combines thermodynamics, phase equilibrium, and process optimization. Specifically, we investigate the process of reconcentrating a water-laden DME stream to realize a circular solvent economy. To this end, we have selected NaCl as a model feed solution to investigate the influence of critical operational parameters, including interstage flash pressure, the number of concentration stages, and the heat source temperature, on the system's energy efficiency and economic viability. This parametric analysis is designed to provide insights that, although

initially focused on NaCl solutions, are anticipated to be applicable to a broader range of inorganic solutions.

Central to this system is the exploitation of DME's unique properties—its low polarity and its ability to form an asymmetric hydrogen bond with water. This synergistic combination facilitates selective water extraction from hypersaline brines, enhancing water solubility over charged ions by a factor of 10^3. The combination of the extended universal quasichemical (eUNIQUAC) model and the virial equation of state within the framework effectively predicts activity and fugacity coefficients, registering mean absolute errors of 2.1 % and 3.2 % when determining compositions at phase equilibrium. Our computational findings suggest that high yield (> 99 %) DME recovery using ultra-low-grade heat sources ($T < 50$ ° C) can be attained with the proposed solvent concentrator. The solvent concentrator within the SDWE system is a key component, facilitating DME recovery through heat-driven concentration stages. Across heat source temperatures ranging from 323 K to 373 K, optimal operation is achieved at interstage flash pressures between 0.4 bar and 0.5 bar, with superior performance observed at lower heat source temperatures. Notably, an optimal thermodynamic efficiency and a minimized specific cost were observed at an interstage pressure of 0.489 bar and a heat source temperature of 323 K, with the specific cost of water production at US$ 1.93 m^{-3}. With a heat source temperature of 323 K and an interstage flash pressure of 0.5 bar, the system attains a DME/water selectivity ratio of approximately 125 and a 99 % recovery rate of DME, with a distillate purity of 99.3 %.

Our preliminary techno-economic analysis underscores the influence of various factors like capital and operating costs, alongside local economic conditions such as interest rates and energy prices, on the system's viability. For example, our analysis indicates that the specific cost of water extraction is most heavily influenced by the local interest rate, as a consequence of its impact on the amortized capital costs. Using the same assumptions in the techno-economic projections, the DME-based SDWE system emerges as a potentially cost-effective and energy-efficient solution for hypersaline brine treatment, achieving comparable specific costs with existing commercial thermal distillation technologies while mitigating the scaling risks on heat and mass exchangers.

To fully realize the capabilities of the DME-based SDWE system, however, several key areas necessitate future investigation. To bridge existing knowledge gaps, understanding the water extraction kinetics between the organic solvent and water in the liquid-liquid separator is crucial, since deviations from the expected liquid-liquid equilibrium may potentially attenuate the thermodynamic and material efficiencies [14]. Further experimental investigation with representative brines and leachates is required to quantify the effects of multicomponent inorganic mixtures on phase compositions at solid-liquid and liquid-liquid equilibrium, due to their significant impact on water's chemical potential and effective dielectric constant [7, 49, 50]. Consequently, the techno-economic viability of DME-driven extraction must be revisited based on empirical data derived from experiments with the representative brines and leachates.

The high volatility of DME, a small organic molecule, poses a risk of leakage through fittings in the solvent concentrator, with potential material losses. Additionally, enhancing heat transfer efficiency in the solvent concentrator is vital, and this suggests opportunities for heat exchanger surfaces with favorable wettability characteristics to DME. Moreover, via gas chromatography - flame ionization detection (GC-FID), our prior experiments on extracting residual DME from water have shown that simply leaving the solution in an open, stationary vessel can substantially lower DME concentrations to between 5 and 50 ppm, suggesting the feasibility of recycling DME via a recovery polishing step that captures the DME removed from the water [91]. This necessitates a comprehensive evaluation of the energy efficiency and cost-effectiveness of various polishing methods, including vacuum application, adsorp-

tion, and membrane processes, aimed at reducing DME leakage and improving system efficiency. Lastly, given the economic sensitivity to the price of low-grade heat, it is imperative to consider local energy costs for more accurate, regionally-specific techno-economic projections.

Appendix A. Scaling Limitations for Hypersaline Brine Concentration

Figure A.8A plots the specific energy (electrical work equivalent) of various water extraction technologies as a function of the concentration of the saline feed [92]. In general, membrane technologies register lower specific energies as a result of the high water selectivity of reverse osmosis membranes and the use of energy recovery devices like pressure exchangers [89, 93]. However, the limitations arising from the high osmotic pressure of concentrated brines restrict most practical use of membranes to feed solutions that are under 70 g L^{-1} [17, 93].

Thermal distillation technologies including multi-effect distillation [22, 78] and multi-stage flash [68] are more tolerant of concentrating brines at higher feed salinities. However, the presence of sparingly soluble inorganic solutes, such as the sulfates and phosphates of calcium and magnesium, poses scaling risks for the heat and mass exchangers in these systems [89, 94, 95]. The deposition of inorganic scales reduces the heat and mass transfer efficacy, raising the energy consumption, lowering the net water recovery, and leading to increased maintenance and operational costs [14, 21, 38].

Solvent-driven water extraction has garnered increased attention in recent years, driven by the need for brine concentration technologies that are less susceptible to the adverse effects from inorganic fouling [7, 9, 14, 24, 32, 34–36, 38, 39, 43, 46, 96]. As illustrated in Fig. A.8B, in solvent-driven water extraction, the organic solvent

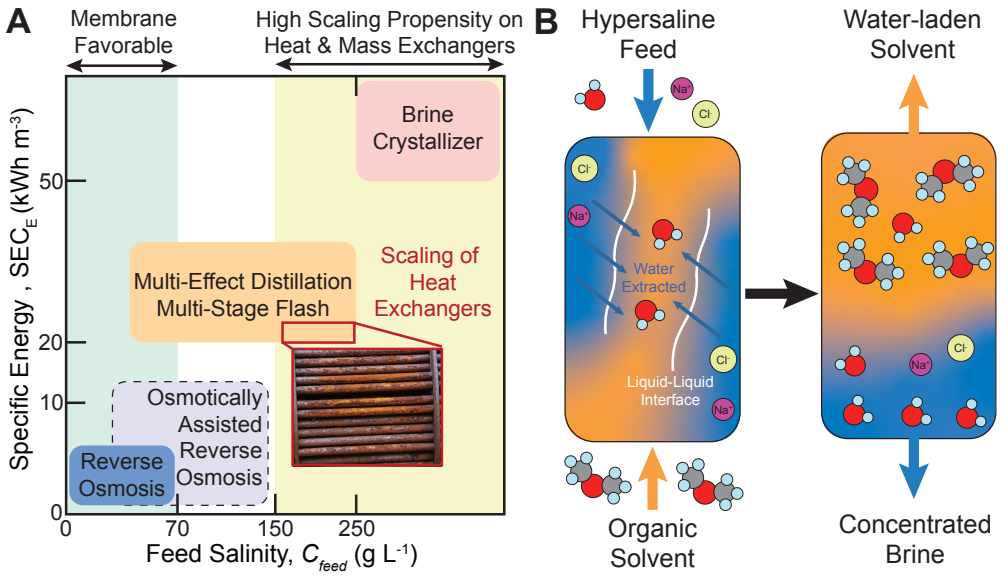

Figure A.8: (A) Specific energy consumption of membrane and thermal desalination technologies as a function of the feed concentration. The specific energy costs of osmotically assisted reverse osmosis is based on computational predictions (dashed boundaries), and have not been demonstrated industrially [17]. The exposure of the heat exchangers to hypersaline brines results in scale deposition, negatively impacting the efficacy of heat transfer [89, 92]. (B) An aprotic solvent extracts water across an organic-aqueous liquid interface into the organic-rich phase, while isolating the charged ions and other potential scalants in the aqueous-rich phase [9, 14, 24, 43]. The near-salt-free water-laden organic phase can be re-concentrated to recover the solvated water.

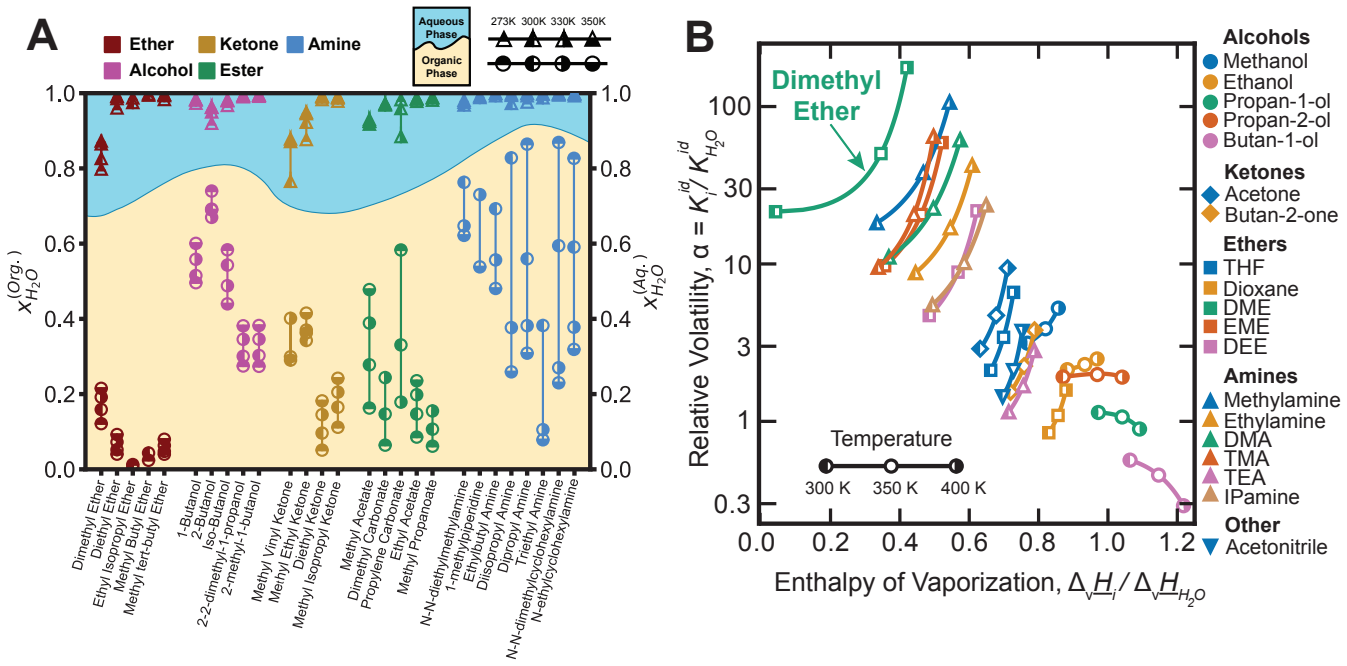

Figure A.9: (A) Composition of both aqueous- and organic-rich phases in binary solvent-water mixtures at liquid-liquid equilibrium (LLE). Specifically, dimethyl ether is noted for its substantial capacity to carry water, reaching up to 22 % by moles in the organic-rich phase at LLE. (B) Plot depicting the relative volatility against the normalized enthalpy of vaporization for various binary solvent-water mixtures. Solvents positioned towards the upper left quadrant of this plot generally indicate higher separation coefficients, suggesting that such solvents can be purified to high degrees at relatively lower temperatures. Notably, dimethyl ether, located in the uppermost left quadrant, is identified as the solvent most efficiently recoverable post liquid-liquid extraction. This figure is adapted from our prior open-access publication [14].

extracts water preferentially into the organic-rich phase, retaining the charged inorganic solutes in the aqueous-rich retentate. Thereafter, the water-laden organic solvent is siphoned out and re-concentrated with a separate process to recover the extracted water. The critical water/salt mass transfer selectivity occurs along the organic-aqueous liquid-liquid interface, isolating the occurrence of inorganic scaling away from the downstream heat and mass exchangers. Consequently, solvent-driven water extraction technology is amenable to feed solutions of much higher concentration, facilitates fractional crystallization of scalants or other target solutes in the bulk solution, and can be potentially leveraged to realize zero-liquid discharge desalination. As illustrated in Fig. A.9A & B, dimethyl ether (DME) emerges as a promising solvent candidate, attributed to its significant water absorption capacity and one of the highest relative volatilities, facilitating easy regeneration after water extraction.

Appendix B. Thermodynamic Fundamentals for Liquid-Liquid and Vapor-Liquid Equilibrium

The First Law of Thermodynamics for a mixture in a microcanonical ensemble undergoing isothermal heat transfer can be expressed as [75]:

$$dU = TdS - pdV + \sum_{i}^{N} \mu_i dN_i \tag{B.1}$$

where U [J], S [J K^{-1}] represent the internal energy and entropy, T [K], P [Pa] and μ_i [J mol^{-1}] represent the temperature, pressure and chemical potential of species i, and V [m^3] and N_i [mol] represent the volume and the molar amount of species i, respectively. The thermodynamic potential in an isobaric-isothermal ensemble (NPT ensemble) can be derived with a Legendre transformation, yielding the Gibbs free energy:

$$dG = d(U + pV - TS) \tag{B.2}$$

$$= dU + pdV + VdP - TdS - SdT \tag{B.3}$$

$$= VdP - SdT + \sum_{i}^{N} \mu_i dN_i \tag{B.4}$$

where G [J] denotes the Gibbs free energy of the mixture. The Second Law of Thermodynamics states that, in an isolated system (i.e., microcanonical ensemble), any spontaneous process will either increase or preserve the entropy of a system [75], as described in Eq. B.5. When the same Legendre transformation is applied, it can be shown that the Gibbs free energy extremum principle applies in the NPT ensemble, as denoted in Eq. B.6 [75].

$$dS_{sys} + dS_{env} \geq 0 \tag{B.5}$$

$$dG_{sys} \leq 0 \tag{B.6}$$

where the subscripts "*sys*" and "*env*" represent the system and the environment, respectively. As a consequence, systems that are in thermodynamic equilibrium in the NPT ensemble would have equal Gibbs free energies [22]. For a two-phase mixture that exists in equilibrium in the NPT ensemble, the Gibbs free energy extremum principle is satisfied by:

$$T^{(phase,1)} = T^{(phase,2)} \tag{B.7}$$

$$P^{(phase,1)} = P^{(phase,2)} \tag{B.8}$$

$$\mu_i^{(phase,1)} = \mu_i^{(phase,2)} \tag{B.9}$$

where i refers to the species that exist in both phases. In the context of liquid-liquid equilibrium, the equal chemical potential constraint can be expressed as:

$$\mu_i^{aq,liq|ref} + RT \ln \left[\gamma_i^{aq,liq}(T, \boldsymbol{x}^{aq,liq})\ x_i^{aq,liq} \right] = \mu_i^{org,liq|ref} + RT \ln \left[\gamma_i^{org,liq}(T, \boldsymbol{x}^{org,liq})\ x_i^{org,liq} \right] \tag{B.10}$$

where $\mu_i^{aq,liq|ref}$ [J mol^{-1}] and $\mu_i^{org,liq|ref}$ [J mol^{-1}] denote the reference chemical potential of species i in the aqueous-rich and organic-rich liquid phases, respectively. If the reference states are chosen to be at the same temperature, pressure and composition, Eq. B.10 simplifies to an isoactivity condition, as expressed by Eq. B.11:

$$\gamma_i^{aq,liq}(T, \boldsymbol{x}^{aq,liq})\ x_i^{aq,liq} = \gamma_i^{org,liq}(T, \boldsymbol{x}^{org,liq})\ x_i^{org,liq} \tag{B.11}$$

In the context of a mixture that exists in vapor-liquid equilibrium, the equality in chemical potential can be expressed as:

$$\mu_i^{liq|ref} + RT \ln \left[\gamma_i^{liq}(T, \boldsymbol{x}^{liq})\ x_i^{liq} \right] = \mu_i^{vap|ref} + RT \ln \left[\frac{f_i^{vap}}{P_i^{sat}} \right] \tag{B.12}$$

where f_i^{vap} [-] $= \phi_i^{vap}(T, P, \boldsymbol{x}^{vap})\ x_i^{vap} P$ denotes the vapor phase fugacity of species i [75]. All together, this gives the isofugacity condition for VLE, as expressed by Eq. B.13:

$$\gamma_i^{liq}(T, \boldsymbol{x}^{liq})\ x_i^{liq} P_i^{sat} = \phi_i^{vap}(T, P, \boldsymbol{x}^{vap})\ x_i^{vap} P \tag{B.13}$$

Table C.1: Interaction parameters for UNIQUAC activity coefficient model.

	$u_{i,i}$	$u_{i,j}$
Dimethyl Ether	−1.23654	332.474
Water	1.20546	−814.698

Appendix C. Phase Compositions at Liquid-Liquid and Vapor-Liquid Equilibrium

Here, the phase compositions of the DME-water mixture at liquid-liquid and vapor-liquid equilibrium are calculated using the eUNIQUAC model and the virial equation of state. The hyperparameters for the UNIQUAC model are regressed with Aspen Hysys and are summarized in Table C.1. The hyperparameters of the virial equation for DME and water are obtained from Tsonopoulous [64, 65].

Fig. 3A illustrates the liquid-liquid equilibrium composition of a ternary mixture of DME, water and NaCl, as a function of the temperature and the NaCl concentration in the brine stream. The model is juxtaposed against the experimental measurements by Holldorff and Knapp [47] and McNally et al. [31]. The eUNIQUAC model converges to the experimental measurements to a high degree, with a mean absolute error of 2.1 %. The composition of the aqueous- and organic-rich liquid phases are denoted by the blue and orange regions, respectively.

From the figure, we observe that the water content of the organic phase increases with temperature, rising from approximately 0.1 at 250 K to approximately 0.21 at 330 K, for the case with $x_{b,i}^{aq} = 0$. However, the presence of NaCl induces a "salting-out effect" across the spectrum of tested temperatures, with the water content in the organic-rich phase reducing from 0.1 to approximately 0.08 at 250 K. This observation aligns with prior phase equilibrium investigations [81–83], and it reflects the reduced solubility of the organic solvent in the aqueous-rich phase.

Fig. 3B illustrates the phase composition of the DME-water mixture at vapor-liquid-equilibrium as a function of the pressure and the mole fractions. The model predictions are juxtaposed against the measurements from Holldorff and Knapp [47] and Pozo et al. [71, 72]. Our model predictions align with the empirical measurements to an average absolute mean error that is under 3.2 %. As observed in Fig. 3B, at a temperature of 293 K, the vapor phase of a DME-water mixture at VLE exhibits an DME-purity that is approximately 99 % or greater. This result reaffirms that high purity DME can be recovered, while employing heat from a low-temperature thermal reservoir.

Appendix D. Numerical Algorithms for System-Scale Analysis

The numerical algorithm employed to simulate the system-scale characteristics is summarized in Fig. D.10. Here, the pink, blue and green bubbles correspond to the inputs, the model, and the outputs. First, the concentration and temperature of the brine and DME streams entering the liquid-liquid separator are inputted into the liquid-liquid equilibrium solver, to derive the composition and temperature of the output streams from the liquid-liquid separator. Thereafter, the concentration and temperature of the water-laden DME-stream, and the number of concentration stages and interstage flash pressure, are inputted into the system flash model. The system flash model employs a constrained trust-region solver to derive the vapor and organic-liquid qualities, and the temperature at VLLE or VLE. The equilibrium temperature and the phase qualities are subsequently leveraged to compute the composition of the retentate and distillate, and the specific electrical and thermal energy consumption. Lastly, the specific thermal

and electrical energy consumption is combined with the knowledge of the heat source temperature, as well as the constituents of the capital and operational costs, to perform techno-economic projections. The techno-economic model returns the specific heat exchanger area, thermodynamic efficiency and the specific cost of water extraction.

Appendix E. Hyperparameters for Techno-economic Projections

We delineate the hyperparameters of the techno-economic model in this section. The techno-economic model is adapted from the recent publications by Chen et al. [21] and Ahdab et al. [3]. First, the capital cost of the solvent concentrator is assumed to scale with the heat exchanger area, following the correlations adopted in the literature [21, 97, 98]. The projected capital cost includes the cost of the pumps, compressors, heat exchangers, throttle valves and pipes that are typical of a multi-effect distillation system [21, 97, 98]. The capital expenditure is amortized over a period of 15 years [3]. The interest rates, labor and electricity costs for six different countries are summarized in Table E.2, based on latest publicly available information as of 15 October 2023. The interest rates correspond to the respective central bank interest rates. The labor costs are derived based on a survey by Economic Research Institute, using the job title "Chemical Engineer" as the query, and the largest populated city of the respective country as the location of work. The electricity cost is derived based on the information available from the public utility departments of the respective countries. The maintenance and chemical costs are assumed to be US$ 0.05 m^{-3} and US$ 0.09 m^{-3}, respectively [21].

Table E.2: Interest rate ane the labor and electricity costs of six countries based on publicly available sources.

	China	United States	Germany	Australia	Brazil	South Africa
Interest Rate (%)	3.45	5.50	4.25	4.10	13.75	8.25
Labor Cost (US$ yr^{-1})	56,780	154,470	102,190	102,620	39,700	60,000
Electricity Cost (US$ kWh^{-1})	0.087	0.142	0.441	0.264	0.140	0.071

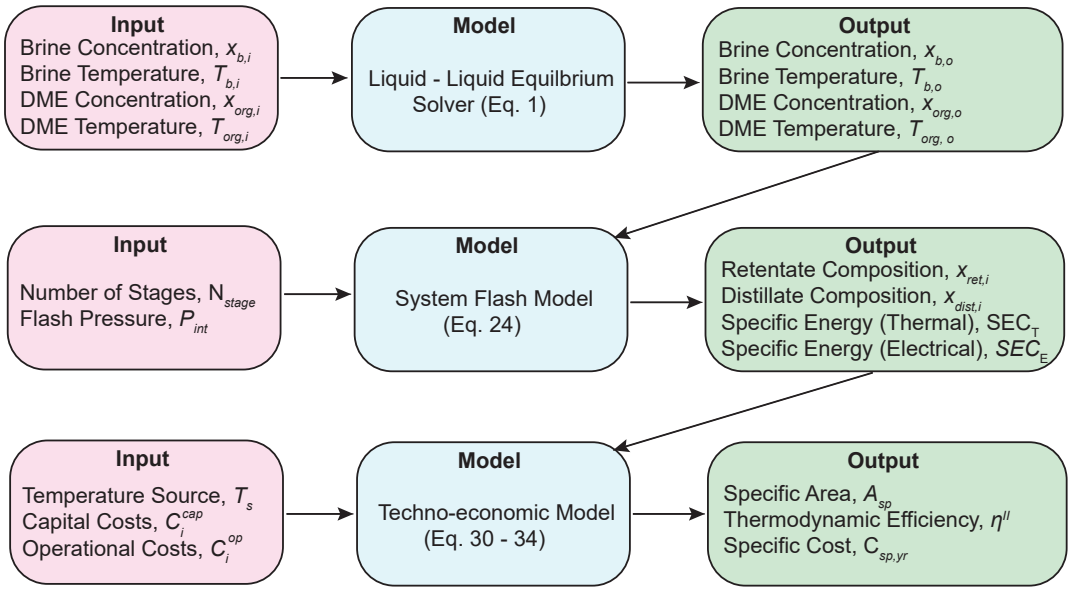

Figure D.10: Numerical algorithm to simulate the system thermodynamic and techno-economic performance.

Nomenclature

Roman Symbols

A	Heat Exchanger Area [m^2]
A_{DH}	Debye Huckel Parameter [$g^{0.5}$ $mol^{-0.5}$]
AF	Annuity Factor [-]
CapEx	Capital Cost [US$]
b_{DH}	Debye Huckel Parameter [$g^{0.5}$ $mol^{-0.5}$]
C	Cost [US$]
G	Molar Gibbs Free Energy [J mol^{-1}]
H	Molar Enthalpy [J mol^{-1}]
I	Ionic Strength [mol m^{-3}]
M	Molecular Weight [g mol^{-1}]
N	Number of Stages [-]
$\dot{N}$	Molar Amount [mol s^{-1}]
OpEx	Operational Cost [US$]
P	Pressure [bar]
Q	Heat Transfer [J]
q	Relative van der Waals Surface Area Parameter [-]
R	Ideal Gas Constant [J mol^{-1} K^{-1}]
r	Relative van der Waals Volume Parameter [-]
S	Molar Entropy [J mol^{-1} K^{-1}]
SEC_E	Specific Energy Consumption - Electrical [kWh mol^{-1}]
SEC_T	Specific Energy Consumption - Thermal [kWh mol^{-1}]
t	Total [-]
T	Temperature [K]
W	Electrical Work [J]
x	Mole Fraction [-]

Greek Symbols

γ	Activity Coefficient [-]
η	Thermodynamic (Second Law) Efficiency [-]
θ	van der Waals Surface Area Fraction Parameter [-]
μ	Chemical Potential [J mol^{-1}]
ξ	Quality [-]
σ	Solvent Recovery [-]
τ	UNIQUAC Interaction Parameter [-]
ϕ	Fugacity Coefficient [-]
ψ	van der Waals Volume Fraction Parameter [-]

ω	Accentricity Factor [-]

Abbreviations

aq	Aqueous
b	Brine
c	Critical Point
$dist$	Distillate
DME	Dimethyl Ether
env	Environment
eq	Equilibrium
i	Species i
in	Input
int	Interstage
is	Isentropic
LLE	Liquid Liquid Equilibrium
mix	Mixture
org	Organic
ret	Retentate
sp	Specific
sys	System
vap	Vapor
VLE	Vapor Liquid Equilibrium
VLLE	Vapor Liquid Liquid Equilibrium
yr	Year

CRediT Authorship Contribution Statement

Zi Hao Foo: Conceptualization, Methodology, Software, Formal Analysis, Writing - Original Draft. **Akshay Deshmukh:** Conceptualization, Methodology. **Aaron D. Wilson:** Supervision, Writing - Review & Editing. **John H. Lienhard:** Conceptualization, Formal Analysis, Supervision, Writing - Review & Editing.

Declaration of Competing Interest

Z.H. Foo, A. Deshmukh, A.D. Wilson and J.H. Lienhard are named inventors on the patent US20220212957B2 assigned to Massachusetts Institute of Technology and Battelle Energy Alliance.

Acknowledgements

This work was supported by the National Alliance for Water Innovation (NAWI) and the Critical Materials Institute (CMI), funded by the US Department of Energy, Office of Energy Efficiency and Renewable Energy,

Advanced Manufacturing Office. The authors acknowledge supplemental support from the MathWorks Fellowship (Z.H. Foo), the NUS Development Grant (Z.H. Foo) and the MIT Energy Initiative Fellowship (A. Deshmukh). Any opinions, findings, and conclusions or recommendations expressed in this material are those of the author(s) and do not necessarily reflect the views of their respective funding agencies.

References

[1] Z. Wang, M. He, H. Jiang, H. He, J. Qi, J. Ma, Photocatalytic MOF membranes with two-dimensional heterostructure for the enhanced removal of agricultural pollutants in water, Chemical Engineering Journal 435 (2022) 133870. doi:10.1016/j.cej.2021.133870.

[2] G. Pérez-Lucas, A. E. Aatik, M. Aliste, V. Hernández, J. Fenoll, S. Navarro, Reclamation of aqueous waste solutions polluted with pharmaceutical and pesticide residues by biological-photocatalytic (solar) coupling in situ for agricultural reuse, Chemical Engineering Journal 448 (2022) 137616. doi:10.1016/j.cej.2022.137616.

[3] Y. D. Ahdab, G. Schücking, D. Rehman, J. H. Lienhard, Cost effectiveness of conventionally and solar powered monovalent selective electrodialysis for seawater desalination in greenhouses, Applied Energy 301 (2021) 117425. doi:10.1016/j.apenergy.2021.117425.

[4] A. E. Zadeh, K. Touati, C. N. Mulligan, J. R. McCutcheon, M. S. Rahaman, Closed-loop pressure retarded osmosis draw solutions and their regeneration processes: A review, Renewable and Sustainable Energy Reviews 159 (2022) 112191. doi:10.1016/j.rser.2022.112191.

[5] J. Jiang, B. Ming, Q. Huang, Y. Guo, J. Shang, J. Jurasz, P. Liu, A holistic techno-economic evaluation framework for sizing renewable power plant in a hydro-based hybrid generation system, Applied Energy 348 (2023) 121537. doi:10.1016/j.apenergy.2023.121537.

[6] B. K. Pramanik, L. D. Nghiem, F. I. Hai, Extraction of strategically important elements from brines: Constraints and opportunities, Water Research 168 (2020) 115149. doi:10.1016/j.watres.2019.115149.

[7] C. Stetson, D. Prodius, H. Lee, C. Orme, B. White, H. Rollins, D. Ginosar, I. C. Nlebedim, A. D. Wilson, Solvent-driven fractional crystallization for atom-efficient separation of metal salts from permanent magnet leachates, Nature Communications 13 (2022) 3789. doi:10.1038/s41467-022-31499-7.

[8] J.-P. Mericq, S. Laborie, C. Cabassud, Evaluation of systems coupling vacuum membrane distillation and solar energy for seawater desalination, Chemical Engineering Journal 166 (2011) 596–606. doi:10.1016/j.cej.2010.11.030.

[9] C. Boo, H. Qi, I. H. Billinge, K. M. Shah, H. Fan, N. Y. Yip, Thermomorphic Hydrophilicity Base-Induced Precipitation for Effective Descaling of Hypersaline Brines, ACS ES&T Engineering 1 (9) (2021) 1351–1359. doi:10.1021/acsestengg.1c00160.

[10] H. T. El-Dessouky, H. M. Ettouney, F. Mandani, Performance of parallel feed multiple ffect evaporation system for seawater desalination, Applied Thermal Engineering 20 (17) (2000) 1679–1706. doi:10.1016/S1359-4311(99)00098-8.

[11] T. Luo, A. Bajpayee, G. Chen, Directional solvent for membrane-free water desalination-A molecular level study, Journal of Applied Physics 110 (5) (2011) 54905. doi:10.1063/1.3627239.

[12] S. Alotaibi, O. M. Ibrahim, Y. Wang, T. Luo, Exergy analysis of directional solvent extraction desalination process, Entropy 21 (3) (2019) 321. doi:10.3390/e21030321.

[13] F. He, H. You, X. Liu, X. Shen, J. Zhang, Z. Wang, Interfacial-heating solar desalination of high-salinity brine: Recent progress on salt management and water production, Chemical Engineering Journal 470 (2023) 1385–8947. doi:10.1016/j.cej.2023.144332.

[14] Z. H. Foo, C. Stetson, E. Dach, A. Deshmukh, H. Lee, A. K. Menon, R. Prasher, N. Y. Yip, J. H. Lienhard, A. D. Wilson, Solvent-driven aqueous separations for hypersaline brine concentration and resource recovery, Trends in Chemistry 4 (12) (2022) 1078–1093. doi:10.1016/j.trechm.2022.09.004.

[15] W. Xie, P. Tang, Q. Wu, C. Chen, Z. Song, T. Li, Y. Bai, S. Lin, A. Tiraferri, B. Liu, Solar-driven desalination and resource recovery of shale gas wastewater by on-site interfacial evaporation, Chemical Engineering Journal 428 (2022) 1385–8947. doi:10.1016/j.cej.2021.132624.

[16] Z. Yuan, H. Liu, W. F. Yong, Q. She, J. Esteban, Status and advances of deep eutectic solvents for metal separation and recovery, Green Chemistry 24 (2022) 1895–1929. doi:10.1039/d1gc03851f.

[17] T. V. Bartholomew, N. S. Siefert, M. S. Mauter, Cost Optimization of Osmotically Assisted Reverse Osmosis, Environmental Science and Technology 52 (20) (2018) 11813–11821. doi:10.1021/acs.est.8b02771.

[18] T. Altmann, J. Robert, A. Bouma, J. Swaminathan, J. H. Lienhard, Primary energy and exergy of desalination technologies in a power-water cogeneration scheme, Applied Energy 252 (2019) 113319. doi:10.1016/j.apenergy.2019.113319.

[19] Z. H. Foo, J. B. Thomas, S. M. Heath, J. A. Garcia, J. H. Lienhard, Sustainable Lithium Recovery from Hypersaline Salt-Lakes by Selective Electrodialysis: Transport and Thermodynamics, Environmental Science and Technology 57 (2023) 14747–14759. doi:10.1021/acs.est.3c04472.

[20] D. M. Miller, K. Abels, J. Guo, K. S. Williams, M. J. Liu, W. A. Tarpeh, Electrochemical Wastewater Refining: A Vision for Circular Chemical Manufacturing, Journal of the American Chemical Society 145 (36) (2023) 19422–19439. doi:10.1021/jacs.3c01142.

[21] Q. Chen, M. Burhan, M. W. Shahzad, D. Ybyraiymkul, F. H. Akhtar, Y. Li, K. C. Ng, A zero liquid discharge system integrating multi-effect distillation and evaporative crystallization for desalination brine treatment, Desalination 502 (2021) 114928. doi:10.1016/j.desal.2020.114928.

[22] K. H. Mistry, M. A. Antar, J. H. Lienhard, An improved model for multiple effect distillation, Desalination and Water Treatment 51 (4-6) (2013) 807–821. doi:10.1080/19443994.2012.703383.

[23] M. M. Kaheal, A. Chiasson, M. Alsehli, Component-based, dynamic simulation of a novel once through multistage flash (MSF-OT) solar thermal desalination plant, Desalination 548 (2023) 116290. doi:10.1016/j.desal.2022.116290.

[24] A. Deshmukh, Z. H. Foo, C. Stetson, H. Lee, C. J. Orme, A. D. Wilson, J. H. Lienhard, Thermodynamics of solvent-driven water extraction from hypersaline brines using dimethyl ether, Chemical Engineering Journal 434 (2022) 134391. doi:10.1016/j.cej.2021.134391.

[25] C. D. Peters, N. P. Hankins, Making zero-liquid discharge desalination greener: Utilising low-grade heat and vacuum membrane distillation for the regeneration of volatile draw solutes, Desalination 507 (2021) 115034. doi:10.1016/j.desal.2021.115034.

[26] Z. H. Foo, D. Rehman, A. T. Bouma, S. Monsalvo, J. H. Lienhard, Lithium Concentration from Salt-Lake Brine by Donnan-Enhanced Nanofiltration, Environmental Science and Technology 57 (2023) 6320–6330. doi:10.1021/acs.est.2c08584.

[27] R. R. Davison, D. W. Hood, Thermodynamic cycles for recovery of water by solvent extraction, Industrial and Engineering Chemistry Process Design and Development 3 (4) (1964) 399–404. doi:10.1021/i260012a023.

[28] R. R. Davison, W. B. Harris, W. H. Smith, A solvent extraction desalination pilot plant, Desalination 3 (1) (1967) 17–26. doi:10.1016/S0011-9164(00)84020-5.

[29] L. Lazare, The puraq seawater desalination process, Desalination 42 (1) (1982) 11–16. doi:10.1016/S0011-9164(00)88736-6.

[30] L. Lazare, The Puraq seawater desalination process - An update, Desalination 85 (3) (1992) 345–360. doi:10.1016/0011-9164(92)80016-3.

[31] J. S. McNally, Z. H. Foo, A. Deshmukh, C. J. Orme, J. H. Lienhard, A. D. Wilson, Solute displacement in the aqueous phase of water-NaCl-organic ternary mixtures relevant to solvent-driven water treatment, RSC Advances 10 (49) (2020) 29516–29527. doi:10.1039/d0ra06361d.

[32] C. Boo, R. K. Winton, K. M. Conway, N. Y. Yip, Membrane-less and Non-Evaporative Desalination of Hypersaline Brines by Temperature Swing Solvent Extraction, Environmental Science and Technology Letters 6 (6) (2019) 359–364. doi:10.1021/acs.estlett.9b00182.

[33] D. B. Sanap, K. D. Kadam, M. Narayan, S. Kasthurirangan, P. R. Nemade, V. H. Dalvi, Analysis of saline water desalination by directed solvent extraction using octanoic acid, Desalination 357 (2015) 150–162. doi:10.1016/j.desal.2014.11.020.

[34] C. Boo, I. H. Billinge, X. Chen, K. M. Shah, N. Y. Yip, Zero Liquid Discharge of Ultrahigh-Salinity Brines with Temperature Swing Solvent Extraction, Environmental Science and Technology 54 (14) (2020) 9124–9131. doi:10.1021/acs.est.0c02555.

[35] K. M. Shah, I. H. Billinge, E. Dach, N. Y. Yip, Advancing the Productivity-Selectivity Trade-off of Temperature Swing Solvent Extraction Desalination with Intermediate-Step Release, Environmental Science & Technology Letters 10 (10) (2023) 949–954. doi:10.1021/acs.estlett.3c00616.

[36] K. M. Shah, E. Dach, R. Winton, H. Fan, N. Y. Yip, Phase equilibria insights into amine-water-NaCl interactions in liquid-liquid biphasic systems for temperature swing solvent extraction desalination, Desalination 548 (2023) 116259. doi:10.1016/j.desal.2022.116259.

[37] A. Bajpayee, T. Luo, A. Muto, G. Chen, Very low temperature membrane-free desalination by directional solvent extraction, Energy and Environmental Science 4 (5) (2011) 1672–1675. doi:10.1039/c1ee01027a.

[38] K. M. Shah, I. H. Billinge, X. Chen, H. Fan, Y. Huang, R. K. Winton, N. Y. Yip, Drivers, challenges, and emerging technologies for desalination of high-salinity brines: A critical review, Desalination 538 (2022) 115827. doi:10.1016/j.desal.2022.115827.

[39] A. D. Wilson, H. Lee, C. Stetson, Local stress within a granular molecular solvent matrix, a mechanism for individual ion hydration, Journal of Molecular Liquids 361 (2022) 119544. doi:10.1016/j.molliq.2022.119544.

[40] J. Guo, Z. D. Tucker, Y. Wang, B. L. Ashfeld, T. Luo, Ionic liquid enables highly efficient low temperature desalination by directional solvent extraction, Nature Communications 12 (1) (2021) 1–7. doi:10.1038/s41467-020-20706-y.

[41] T. Hanada, M. Goto, Synergistic Deep Eutectic Solvents for Lithium Extraction, ACS Sustainable Chemistry and Engineering 9 (5) (2021) 2152–2160. doi:10.1021/acssuschemeng.0c07606.

[42] G. D. Barbosa, J. E. Bara, S. T. Weinman, C. H. Turner, Molecular aspects of temperature swing solvent extraction for brine desalination using imidazole-based solvents, Chemical Engineering Science 247 (2022) 116866. doi:10.1016/j.ces.2021.116866.

[43] G. D. Barbosa, X. Liu, J. E. Bara, S. T. Weinman, C. H. Turner, High-salinity brine desalination with amine-based temperature swing solvent extraction: A molecular dynamics study, Journal of Molecular Liquids 341 (2021) 117359. doi:10.1016/j.molliq.2021.117359.

[44] X. Wu, Z. Lei, Q. Li, J. Zhu, B. Chen, Liquid-liquid extraction of low-concentration aniline from aqueous solutions with salts, Industrial and Engineering Chemistry Research 49 (6) (2010) 2581–2588. doi:10.1021/ie9012979.

[45] R. S. Prasher, A. Z. Haddad, A. K. Menon, H. Kang, J. J. Urban, R. Kostecki, Solar Desalination Using Thermally Responsive Ionic Liquids Regenerated with a Photonic Heater, Environmental Science and Technology 55 (5) (2021) 3260–3269. doi:10.1021/acs.est.0c06232.

[46] A. D. Wilson, Z. H. Foo, A. S. Jayasinghe, C. Stetson, H. Lee, H. W. Rollins, A. Deshmukh, J. H. Lienhard, Modeling Henry's law and phase separations of water–NaCl–organic mixtures with solvation and ion-pairing, Physical Chemistry Chemical Physics 26 (2024) 749–759. doi:10.1039/D3CP02003G.

[47] H. Holldorff, H. Knapp, Binary vapor-liquid-liquid equilibrium of dimethyl ether - water and mutual solubilities of methyl chloride and water: Experimental results and data reduction, Fluid Phase Equilibria 44 (2) (1988) 195–209. doi:10.1016/0378-3812(88)80111-0.

[48] A. A. Monjezi, H. B. Mahood, A. N. Campbell, Regeneration of dimethyl ether as a draw solute in forward osmosis by utilising thermal energy from a solar pond, Desalination 415 (2017) 104–114. doi:10.1016/j.desal.2017.03.034.

[49] Q. Zheng, M. Watanabe, Advances in low-temperature extraction of natural resources using liquefied dimethyl ether, Resources Chemicals and Materials 1 (2022) 16–26. doi:10.1016/j.recm.2022.01.001.

[50] A. S. Jayasinghe, C. Stetson, C. J. Orme, M. Shi, A. D. Wilson, Experimental study of mechanistic factors influencing solvent-driven fractional crystallization of calcium sulfate, Desalination 579 (2024) 117474. doi:10.1016/j.desal.2024.117474.

[51] M. C. Bauer, A. Kruse, The use of dimethyl ether as an organic extraction solvent for biomass applications in future biorefineries: A user-oriented review, Fuel 254 (2019). doi:10.1016/j.fuel.2019.115703.

[52] F. H. Vermeire, W. H. Green, Transfer learning for solvation free energies: From quantum chemistry to experiments, Chemical Engineering Journal 418 (2021) 129307. doi:10.1016/j.cej.2021.129307.

[53] Y. Q. Luo, F. Song, J. M. Wu, F. Wang, X. L. Wang, Y. Z. Wang, A nature-inspired suspended solar evaporator for water desalination of high-salinity brines, Chemical Engineering Journal 421 (2021) 129824. doi:10.1016/j.cej.2021.129824.

[54] S. Hur, S. Kim, H.-S. Kim, A. Kumar, C. Kwon, J. Shin, H. Kang, H. Sung, J. Ryu, J. M. Baik, H.-C. Song, Low-grade waste heat recovery scenarios: Pyroelectric, thermomagnetic, and thermogalvanic thermal energy harvesting, Nano Energy 114 (2023) 108596. doi:10.1016/j.nanoen.2023.108596.

[55] B. E. Fil, S. Garimella, Waste heat recovery in commercial gas-fired tumble dryers, Energy 218 (2020) 119407. doi:10.1016/j.energy.2020.119407.

[56] C. Che, Y. Yin, Improvement of low-grade heat utilization: Sensitivity mechanism of saturated vapor pressure-temperature in dehumidified materials, Applied Thermal Engineering 230 (2023) 120788. doi:10.1016/j.applthermaleng.2023.120788.

[57] R. Law, A. Harvey, D. Reay, Techno-economic comparison of a high-temperature heat pump and an organic Rankine cycle machine for low-grade waste heat recovery in UK industry, International Journal of Low-Carbon Technologies 8 (2013) i47–i54. doi:10.1093/ijlct/ctt029.

[58] J. Andrés-Mañas, L. Roca, A. Ruiz-Aguirre, F. Acién, J. Gil, G. Zaragoza, Application of solar energy to seawater desalination in a pilot system based on vacuum multi-effect membrane distillation, Applied Energy 258 (2020) 114068. doi:10.1016/j.apenergy.2019.114068.

[59] Z. Y. Xu, R. Z. Wang, C. Yang, Perspectives for low-temperature waste heat recovery, Energy 176 (2019) 1037 – 1043. doi:10.1016/j.energy.2019.04.001.

[60] T. Gilbert, A. K. Menon, C. Dames, R. Prasher, Heat source and application-dependent levelized cost of decarbonized heat, Joule 7 (2023) 128–149. doi:10.1016/j.joule.2022.11.006.

[61] K. Thomsen, P. Rasmussen, R. Gani, Correlation and prediction of thermal properties and phase behaviour for a class of aqueous electrolyte systems, Chemical Engineering Science 51 (14) (1996) 3675–3683. doi:10.1016/0009-2509(95)00418-1.

[62] M. C. Iliuta, K. Thomsen, P. Rasmussen, Extended UNIQUAC model for correlation and prediction of vapour-liquid-solid equilibria in aqueous salt systems containing non-electrolytes. Part A. methanol-water-salt systems, Chemical Engineering Science 55 (14) (2000) 2673–2686. doi:10.1016/S0009-2509(99)00534-5.

[63] K. Thomsen, M. C. Iliuta, P. Rasmussen, Extended UNIQUAC model for correlation and prediction of vapor-liquid-liquid-solid equilibria in aqueous salt systems containing non-electrolytes. Part B. Alcohol (ethanol, propanols, butanols)-water-salt systems, Chemical Engineering Science 59 (17) (2004) 3631–3647. doi:10.1016/j.ces.2004.05.024.

[64] C. Tsonopoulos, J. H. Dymond, Second virial coefficients of normal alkanes, linear 1-alkanols (and water), alkyl ethers, and their mixtures, Fluid Phase Equilibria 133 (1-2) (1997) 11–34. doi:10.1016/s0378-3812(97)00058-7.

[65] C. Tsonopoulos, An empirical correlation of second virial coefficients, AIChE Journal 20 (2) (1974) 263–272. doi:10.1002/aic.690200209.

[66] Z. H. Foo, D. Rehman, O. Z. Coombs, A. Deshmukh, J. H. Lienhard, Multicomponent Fickian solution-diffusion model for osmotic transport through membranes, Journal of Membrane Science 640 (2021) 119819. doi:10.1016/j.memsci.2021.119819.

[67] P. Virtanen, R. Gommers, T. E. Oliphant, M. Haberland, T. Reddy, D. Cournapeau, E. Burovski, P. Peterson, W. Weckesser, J. Bright, S. J. van der Walt, M. Brett, J. Wilson, K. J. Millman, N. Mayorov, A. R. Nelson, E. Jones, R. Kern, E. Larson, C. J. Carey, Poİat, Y. Feng, E. W. Moore, J. VanderPlas, D. Laxalde, J. Perktold, R. Cimrman, I. Henriksen, E. A. Quintero, C. R. Harris, A. M. Archibald, A. H. Ribeiro, F. Pedregosa, P. van Mulbregt, A. Vijaykumar, A. P. Bardelli, A. Rothberg, A. Hilboll, A. Kloeckner, A. Scopatz, A. Lee, A. Rokem, C. N. Woods, C. Fulton, C. Masson, C. Häggström, C. Fitzgerald, D. A. Nicholson, D. R. Hagen, D. V. Pasechnik, E. Olivetti, E. Martin, E. Wieser, F. Silva, F. Lenders, F. Wilhelm, G. Young, G. A. Price, G. L. Ingold, G. E. Allen, G. R. Lee, H. Audren, I. Probst, J. P. Dietrich, J. Silterra, J. T. Webber, J. Slavič, J. Nothman, J. Buchner, J. Kulick, J. L. Schönberger, J. V. de Miranda Cardoso, J. Reimer, J. Harrington, J. L. C. Rodríguez, J. Nunez-Iglesias, J. Kuczynski, K. Tritz, M. Thoma, M. Newville, M. Kümmerer, M. Bolingbroke, M. Tartre, M. Pak, N. J. Smith, N. Nowaczyk, N. Shebanov, O. Pavlyk, P. A. Brodtkorb, P. Lee, R. T. McGibbon, R. Feldbauer, S. Lewis, S. Tygier, S. Sievert, S. Vigna, S. Peterson, S. More, T. Pudlik, T. Oshima, T. J. Pingel, T. P. Robitaille, T. Spura, T. R. Jones, T. Cera, T. Leslie, T. Zito, T. Krauss, U. Upadhyay, Y. O. Halchenko, Y. Vázquez-Baeza, SciPy 1.0: fundamental algorithms for scientific computing in Python, Nature Methods 17 (3) (2020) 261–272. doi:10.1038/s41592-019-0686-2.

[68] Y. Roy, G. P. Thiel, M. A. Antar, J. H. Lienhard, The effect of increased top brine temperature on the performance and design of OT-MSF using a case study, Desalination 412 (2017) 32–38. doi:10.1016/j.desal.2017.02.015.

[69] A. Baccioli, M. Antonelli, U. Desideri, A. Grossi, Thermodynamic and economic analysis of the integration of Organic Rankine Cycle and Multi-Effect Distillation in waste-heat recovery applications, Energy 161 (2018) 456–469. doi:10.1016/j.energy.2018.07.150.

[70] A. A. Abdulwahid, H. Zhao, Z. Wang, G. Liu, E. E. Khalil, Y. Lai, J. Han, Thermo-economic comparison of two models of combined transcritical CO 2 refrigeration and multi-effect desalination system , Applied Energy 308 (2021) 118320. doi:10.1016/j.apenergy.2021.118320.

[71] M. E. Pozo, W. B. Streett, Fluid phase equilibria in the system dimethyl ether/water from 50 to 220 C and pressures to 500 bar, Fluid Phase Equilibria 14 (C) (1983) 219–224. doi:10.1016/0378-3812(83)80128-9.

[72] M. E. Pozo, W. B. Streett, Fluid Phase Equilibria for the System Dimethyl Ether/Water from 50 to 220°c and Pressures to 50.9 MPa, Journal of Chemical and Engineering Data 29 (3) (1984) 324–329. doi:10.1021/je00037a030.

[73] J. Wu, Y. Zhou, E. W. Lemmon, An Equation of State for the Thermodynamic Properties of Dimethyl Ether, Journal of Physical and Chemical Reference Data 40 (2) (2011). doi:10.1063/1.3582533.

[74] E. W. Lemmon, M. L. Huber, M. O. McLinden, NIST Standard Reference Database 23: Reference Fluid Thermodynamic and Transport Properties-REFPROP, Version 9.1, National Institute of Standards and Technology (2013). doi:10.18434/T4/1502528.

[75] S. Sandler, Chemical, Biochemical, and Engineering Thermodynamics, 5th Edition, Wiley, 2017.

[76] M. A. Jamil, S. M. Zubair, On thermoeconomic analysis of a single-effect mechanical vapor compression desalination system, Desalination 420 (2017) 292–307. doi:10.1016/j.desal.2017.07.024.

[77] H. Zhang, Z. Zhang, L. Tong, J. Yang, L. Wang, Y. Song, Z. Yu, Y. Zhang, J. Zhang, A mechanical vapor compression regeneration system of potassium formate solution: Model development, experimental verification and performance prediction, Desalination 539 (2022) 115940. doi:10.1016/j.desal.2022.115940.

[78] O. A. Hamed, A. M. Zamamiri, S. Aly, N. Lior, Thermal performance and exergy analysis of a thermal vapor compression desalination system, Energy Conversion and Management 37 (4) (1996) 379–387. doi:10.1016/0196-8904(95)00194-8.

[79] K. C. Ng, K. Thu, S. J. Oh, L. Ang, M. W. Shahzad, A. B. Ismail, Recent developments in thermally-driven seawater desalination: Energy efficiency improvement by hybridization of the MED and AD cycles, Desalination 356 (2015) 255–270. doi:10.1016/j.desal.2014.10.025.

[80] J. M. Weinand, G. Vandenberg, S. Risch, J. Behrens, N. Pflugradt, J. Linßen, D. Stolten, Low-carbon lithium extraction makes deep geothermal plants cost-competitive in future energy systems, Advances in Applied Energy 11 (2023) 100148. doi:10.1016/j.adapen.2023.100148.

[81] S. Endo, A. Pfennigsdorff, K. U. Goss, Salting-out effect in aqueous NaCl solutions: Trends with size and polarity of solute molecules, Environmental Science and Technology 46 (3) (2012) 1496–1503. doi:10.1021/es203183z.

[82] X. Lu, P. Han, Y. Zhang, Y. Wang, J. Shi, Salting-out separation and liquid–liquid equilibrium of tertiary butanol aqueous solution, Chemical Engineering Journal 78 (2-3) (2000) 165–171. doi:10.1016/S1385-8947(00)00153-4.

[83] M. Li, B. Zhuang, Y. Lu, L. An, Z.-G. Wang, Salt-Induced Liquid–Liquid Phase Separation: Combined Experimental and Theoretical Investigation of Water–Acetonitrile–Salt Mixtures, Journal of the American Chemical Society 143 (2) (2021) 773–784. doi:10.1021/jacs.0c09420.

[84] Y. Shi, C. Zhang, R. Li, S. Zhuo, Y. Jin, L. Shi, S. Hong, J. Chang, C. Ong, P. Wang, Solar Evaporator with Controlled Salt Precipitation for Zero Liquid Discharge Desalination, Environmental Science and Technology 52 (2018) 1182211830. doi:10.1021/acs.est.8b03300.

[85] D. M. Davenport, A. Deshmukh, J. R. Werber, M. Elimelech, High-Pressure Reverse Osmosis for Energy-Efficient Hypersaline Brine Desalination: Current Status, Design Considerations, and Research Needs, Environmental Science and Technology Letters 5 (8) (2018) 467–475. doi:10.1021/acs.estlett.8b00274.

[86] Z. Wang, A. Deshmukh, Y. Du, M. Elimelech, Minimal and zero liquid discharge with reverse osmosis using low-salt-rejection membranes, Water Research 170 (2020). doi:10.1016/j.watres.2019.115317.

[87] K. Kurihara, M. Nakamichi, K. Kojima, Isobaric Vapor-Liquid Equilibria for Methanol + Ethanol + Water and the Three Constituent Binary Systems, Journal of Chemical and Engineering Data 38 (3) (1993) 446–449. doi:10.1021/je00011a031.

[88] K. Kurihara, T. Minoura, K. Takeda, K. Kojima, Isothermal Vapor-Liquid Equilibria for Methanol + Ethanol + Water, Methanol + Water, and Ethanol + Water, Journal of Chemical and Engineering Data 40 (3) (1995) 679–684. doi:10.1021/je00019a033.

[89] J. Kim, K. Park, D. R. Yang, S. Hong, A comprehensive review of energy consumption of seawater reverse osmosis desalination plants, Applied Energy 254 (2019). doi:10.1016/j.apenergy.2019.113652.

[90] A. T. Bouma, Q. J. Wei, J. E. Parsons, J. Buongiorno, J. H. Lienhard, Energy and water without carbon: Integrated desalination and nuclear power at Diablo Canyon, Applied Energy (2022). doi:10.1016/j.apenergy.2022.119612.

[91] H. Lee, C. Stetson, C. J. Orme, M. W. Kuns, J. A. Lacey, L. Vega-Montoto, S. W. Snyder, J. R. Wilbanks, J. L. Bowen, A. D. Wilson, Class-based separations of mixed solid-liquid systems with condensable solvent washing and extraction: The dilemma of pizza box recycling, Journal of Cleaner Production 426 (2023). doi:10.1016/j.jclepro.2023.139080.

[92] T. Tong, M. Elimelech, The Global Rise of Zero Liquid Discharge for Wastewater Management: Drivers, Technologies, and Future Directions, Environmental Science and Technology 50 (13) (2016) 6846–6855. doi:10.1021/acs.est.6b01000.

[93] Z. Wang, D. Feng, Y. Chen, D. He, M. Elimelech, Comparison of Energy Consumption of Osmotically Assisted Reverse Osmosis and Low-Salt-Rejection Reverse Osmosis for Brine Management, Environmental Science & Technology 55 (15) (2021) 10714–10723. doi:10.1021/acs.est.1c01638.

[94] H. Lugo-Granados, M. Picón Núñez, Modelling scaling growth in heat transfer surfaces and its application on the design of heat exchangers, Energy 160 (2018) 845–854. doi:10.1016/j.energy.2018.07.059.

[95] S. Kazi, G. Duffy, X. Chen, Mineral scale formation and mitigation on metals and a polymeric heat exchanger surface, Applied Thermal Engineering 30 (14-15) (2010) 2236–2242. doi:10.1016/j.applthermaleng.2010.06.005.

[96] G. D. Barbosa, E. Dach, X. Liu, N. Y. Yip, C. H. Turner, Computational and experimental study of different brines in temperature swing solvent extraction desalination with amine solvents, Desalination 537 (2022) 115863. doi:10.1016/j.desal.2022.115863.

[97] S. Al-Hengari, W. ElMoudir, M. A. El-Bousiffi, Economic assessment of thermal desalination processes, Desalination and Water Treatment 55 (9) (2015) 2423–2436. doi:10.1080/19443994.2014.957982.

[98] M. L. Elsayed, O. Mesalhy, R. H. Mohammed, L. C. Chow, Transient and thermo-economic analysis of MED-MVC desalination system, Energy 167 (2019) 283–296. doi:10.1016/j.energy.2018.10.145.